Heliyon 10 (2024) e29907

Contents lists available at ScienceDirect

Heliyon

journal homepage: www.cell.com/heliyon

Research article

Green and sustainable use of macadamia nuts as support material in Pt-based direct methanol fuel cells

N.A. Mojapelo [a], N.S. Seroka [a,b,*], L. Khotseng [a,**]

[a] Department of Chemistry, University of the Western Cape, Private Bag X17, Bellville, 7535, South Africa
[b] Energy Centre, Smart Places Cluster, Council for Science and Industrial Research (CSIR), Pretoria, 0001, South Africa

ARTICLE INFO

Keywords:
Green chemistry
Macadamia nuts
Biowaste
Pt electrocatalysts
Direct methanol fuel cell

ABSTRACT

The successful commercialization of direct methanol fuel cells (DMFCs) is hindered by inadequate methanol oxidation activity and anode catalyst longevity. Efficient and cost-effective electrode materials are imperative in the widespread use of DMFCs. While Platinum (Pt) remains the primary component of anodic methanol oxidation reaction (MOR) electrocatalysts, its utilization alone in DMFC systems is limited due to carbon monoxide (CO) poisoning, instability, methanol crossover, and high cost. These limitations impede the economic feasibility of Pt as an electrocatalyst. Herein, we present the use of powdered activated carbon (PAC) and granular activated carbon (GAC), both sourced from macadamia nut shells (MNS), a type of biomass. These bio-based carbon materials are integrated into hybrid supports with reduced graphene oxide (rGO), aiming to enhance the performance and reduce the production cost of the Pt electrocatalyst. Electrochemical and physicochemical characterizations of the synthesized catalysts, including Pt-rGO/PAC-1:1, Pt-rGO/PAC-1:2, Pt-rGO/GAC-1:1, and Pt-rGO/GAC-1:2, were conducted. X-ray diffraction analysis revealed crystallite sizes ranging from 1.18 nm to 1.68 nm. High-resolution transmission electron microscopy (HRTEM) images with average particle sizes ranging from 1.91 nm to 2.72 nm demonstrated spherical dispersion of Pt nanoparticles with some agglomeration across all catalysts. The electrochemical active surface area (ECSA) was determined, with Pt-rGO/GAC-1:1 exhibiting the highest ECSA of 73.53 $m^2\ g^{-1}$. Despite its high ECSA, Pt-rGO/GAC-1:1 displayed the lowest methanol oxidation reaction (MOR) current density, indicating active sites with poor catalytic efficiency. Pt-rGO/PAC-1:1 and Pt-rGO/PAC-1:2 exhibited the highest MOR current densities of 0.77 $mA*cm^{-2}$ and 0.74 $mA*cm^{-2}$, respectively. Moreover, Pt-rGO/PAC-1:2 and Pt-rGO/PAC-1:1 demonstrated superior electrocatalytic mass (specific) activities of 7.55 mA/mg (0.025 $mA*cm^{-2}$) and 7.25 mA/mg (0.021 $mA*cm^{-2}$), respectively. Chronoamperometry tests revealed Pt-rGO/PAC-1:2 and Pt-rGO/PAC-1:1 as the most stable catalysts. Additionally, they exhibited the lowest charge transfer resistances and highest MOR current densities after durability tests, highlighting their potential for DMFC applications. The synthesized Pt supported on PACs hybrids demonstrated remarkable catalytic performance, stability, and CO tolerance, highlighting their potential for enhancing DMFC efficiency.

* Corresponding author. Department of Chemistry, University of the Western Cape, Private Bag X17, Bellville, 7535, South Africa.
** Corresponding author.
E-mail addresses: 3754640@myuwc.ac.za (N.S. Seroka), lkhotseng@uwc.ac.za (L. Khotseng).

https://doi.org/10.1016/j.heliyon.2024.e29907
Received 17 January 2024; Received in revised form 16 April 2024; Accepted 17 April 2024
Available online 25 April 2024

1. Introduction

The demand for energy is expected to double by 2050 as a result of the increasing global population, industrialization, and the fourth industrial revolution (4IR) [1]. Fossil fuels are currently the world's main source of energy; however, the utilization of fossil fuels has severe consequences, such as the greenhouse effect (CO_x, NO_x, SO_x), acid rain, ozone layer depletion, water pollution, and more [2–4]. Furthermore, the fast consumption of these non-renewable reservoirs tempts researchers to investigate novel renewable energy and clean energy technologies such as fuel cells, solar, wind, biomass, *etc* [5].

Amongst the discovered renewable energy sources, fuel cells have been identified as the most viable option, due to their intriguing potential to produce energy with high efficiency, density, and cleanness from a range of fuels [6]. Fuel cells are electrochemical devices that generate electricity through electro-catalytic reactions by combining fuel (e.g., hydrogen, alcohol, etc.) with oxygen from the air. The first fuel cell was invented in 1838 by Sir William Robert Groven but the use of fuel cells began in the 1950s by General Electric (GE) company [7,8]. Fuel cells are widely used in various sectors, including telecommunications, portable electronic systems, transportation, and low power devices [8]. These cells can be categorized according to the electrolyte and fuel they use.

Currently, there is a lot of interest in the advancement of fuel cell technology. Various types of fuel cells exist, with examples of low-temperature fuel cells including the proton exchange membrane fuel cell (PEMFC), alkaline fuel cell (AFC), direct methanol fuel cell (DMFC), and phosphoric acid fuel cell (PAFC), whereas high-temperature fuel cell examples include the molten carbonate fuel cell (MCFC) and solid oxide fuel cell (SOFC). Among them, the direct methanol fuel cell (DMFC) stands out due to its low temperature requirement, low-cost, high-power density, rapid refuelling, and minimal environmental impact [9–13].

DMFC directly converts chemical energy in methanol to electrical energy. The most essential component of a DMFC is the membrane electrode assembly (MEA), where the anodic and cathodic reactions occur to produce electrical energy. In DMFC, methanol is supplied as fuel and undergoes oxidation on the anode catalyst, facilitated by the presence of water. This oxidation process results in the production of carbon dioxide, protons, and electrons, as described in Equation (1). Simultaneously, oxygen is reduced on the cathode catalyst, with protons diffusing from the anode through the membrane and electrons traveling through the circuit, as indicated in Equation (2). The thermodynamic potential of DFC is 1.21 V at 25 °C, as shown in Equation (3). These reactions are detailed as follows [14]:

$$\text{Anode}: CH_3OH + H_2O \longrightarrow CO_2 + 6H^+ + 6e^-, E^0 = 0.016\text{V (vs.SHE)} \quad (1)$$

$$\text{Cathode}: 3/2O_2 + 6H^+ + 6e^- \longrightarrow 3H_2O, E^0 = 1.229\text{V (vs.SHE)} \quad (2)$$

$$\text{Overall}: CH_3OH + 3/2O_2 \longrightarrow CO_2 + 2H_2O, E^0 = 1.213\text{V (vs.SHE)} \quad (3)$$

Despite DMFCs being highly recommended as a potential solution to the world's energy crisis due to its high energy-conversion efficiency and low pollution emission, there are still problems that need to be resolved to allow the full commercialization of DMFCs. One major challenge in utilizing DMFCs is the development of low-cost electrocatalysts that are highly active and durable for the two main reactions involved: the methanol oxidation reaction (MOR) occurring at the anode, and the oxygen reduction reaction (ORR) taking place at the cathode. Traditional catalysts such as platinum group metals (Ir, Os, Pt, Pd, Ru, and Rh), as well as Au, Ag, and other noble metals, are chemically stable and have high catalytic activity. However, despite the desirable electrochemical properties exhibited by these catalysts, their low efficiency and high cost still limit the commercialization of the DMFCs [15,16]. Pt alone in a DMFC system suffers from CO poisoning, methanol crossover, and long-term instability due to particle aggregation, dissolution, and the expensive cost of the Pt catalyst limits its economic application as an electrocatalyst. As a result, the kinetic rate of MOR and ORR in the DMFC system is reduced [17,18].

To overcome these issues, carbon nanomaterials have been widely used as catalyst support materials in low temperature fuel cells such as DMFCs. Carbon materials are extensively utilized as supports for catalysts due to their unique properties, which include stability in both acidic and basic electrolytes, excellent conductivity, and the ability to provide a large surface area for the dispersion of metal catalysts. It is believed that carbon materials have a significant impact on the properties of electrocatalysts, such as the size and shape of metal particles, the dispersion of metals, the degree of alloying, and overall stability. Additionally, carbon supports can influence the performance of supported catalysts in fuel cells by affecting mass transport, electronic conductivity in the catalyst layer, electrochemically active area, and the stability of metal nanoparticles during operation [19]. However, the commercialized platinum supported on carbon (Pt/C) catalysts still suffers from drawbacks such as high cost, poor stability, and low Pt utilization rate [20,21]. Additionally, carbon black (CB) is widely used as a support material for Pt due to its remarkable surface area and strong electronic conductivity. However, CB's lower graphitic content, predominant microporous, and reduced electrochemical stability make it susceptible to corrosion, leading to agglomeration/detachment of Pt nanoparticles and consequently reducing catalytic efficiency [22].

Researchers explored innovative methods of utilizing the unique physical and chemical properties of carbon materials. By which Pt-based catalysts supported on novel carbon materials such as mesoporous carbon, carbon cloth (CC), carbon fibers (CFs), carbon quantum dot (CQDs), and carbon nanotubes (CNTs) were used. However, despite some astonishing advantages, these novel carbon materials exhibit drawbacks such as poor stability, weak ability to anchor Pt NPs, and limited surface area. Furthermore, they are prone to corrosion in special environments, resulting in a tremendous decrease in porosity, surface area, and electrochemical performance [23,24]. While others proposed the use of graphene and its derivatives, characterized by sp^2-hybridized carbon atoms with high structural stability, excellent heat resistance, large surface area, and good electrical conductivity, hence, a promising support material for Pt-based catalysts [25]. Despite their enhanced catalytic performance compared to traditional catalysts,

graphene-supported Pt still faces challenges like Pt nanoparticle agglomeration and graphene sheet restacking, along with insufficient conductivity, toxicity resistance, and stability for commercial use [26,27].

To enhance the physical and chemical properties of carbon supports under the conditions of DMFCs operation, materials using higher graphitic nature like graphene integrated with macadamia nut shells (MNS) have been studied in this paper. The presence of microstructures in MNS can improve the electrochemical performance by creating additional pathways for the rapid diffusion of ions. The micropores and mesopores in MNS contribute to its high surface area and pore volume, crucial for ion storage, transportation, and electrolyte penetration. This attribute also enables the material to improve the stability of catalysts and provide various active sites for various reactions that take place on the catalyst surface within the DMFCs. MNS has various applications including in low-temperature fuel cells, making it a promising biobased carbonaceous material for Pt electrocatalyst support [28]. In this project, macadamia nut shells (MNS) are identified as a promising source of biobased carbonaceous material due to their high carbon content, low cost, and reduced environmental impact [29–31]. When Pt electrocatalysts are supported on biobased carbonaceous materials, the resulting composite material exhibits improved properties such as increased surface area, higher conductivity, and enhanced stability.

2. Experimental details

2.1. Reagents and materials

Graphite powder, $NaNO_3$, H_2PtCl_6, and NaOH were purchased from Sigma Aldrich. H_2SO_4, $KMnO_4$, Ethylene glycol, H_2O_2, CH_3OH, and $HClO_4$ were purchased from Kimix. The Nafion solution and isopropanol were purchased from Alfa Aesar. Water was purified by a Mikki-Q system. All chemicals were used as received, without further purifications.

2.2. Preparation of graphene oxide (GO)

Graphene oxide (GO) was prepared according to the modified Hummers' method reported by Hidayat et al. [32]. However, few modifications were made to make the procedure as simple as possible. Approximately 1 g of graphite flake powder, 0.5 g of sodium nitrate ($NaNO_3$) and 50 mL of sulphuric acid (H_2SO_4) were mixed in a 250 mL beaker in a 0 °C ice bath. About 3 g of potassium permanganate ($KMnO_4$) was slowly added into the solution every 30 min, three times in total. During the addition of potassium permanganate ($KMnO_4$) the solution changed colour from black to green. The beaker was then removed from the ice bath and 46 mL of hot de-ionized water was added into the solution dropwise, to avoid an explosion. The addition of hot-deionized water changed the colour of the solution to brownish. The brownish solution was then placed in an oil bath and heated at 90 °C for 60 min. Once the 60 min had elapsed, 20 mL of hydrogen peroxide (H_2O_2) was added to the solution to stop further oxidation. The solution was allowed to cool to room temperature and then sonicated for 30 min. After sonication, the brown solution was centrifuged for 15 min, and a mud-like substance was formed. The material was washed with de-ionized water then a solution of 50 mL of de-ionized water and 50 mL ethanol. The obtained product was then dried at 70 °C in an oven overnight.

2.3. Preparation of reduced graphene oxide (rGO)

The carbonyl reduction method was used to prepare reduced graphene oxide (rGO). The as-prepared GO was placed in a large crucible and then placed in a muffle furnace set to 250 °C with a ramping rate 23 °C/min for 3 h. After 3 h the sample was allowed to cool to room temperature.

2.4. Preparation of bio-based hybrid support materials

Four hybrid support materials of reduced graphene oxide with powdered activated carbon (PAC), and reduced graphene oxide with granular activated carbon (GAC) of different ratio (1:1 & 1:2) were synthesized using the hydrothermal method. For the 1:1 ratio, about 0.500 g of reduced graphene oxide and 0.500 g of powdered/granular activated carbon were mixed with 100 mL of ethylene glycol in a 250 mL beaker. For the 1:2 ratio, approximately 0.5 00 g of reduced graphene oxide and 1 g of powdered/granular activated carbon were dissolved in 100 mL of ethylene glycol in a 250 mL beaker. The solutions were placed in separate Teflon lined autoclaves, and then the autoclaves were placed in a muffle furnace set to 180 °C for 3 h with a ramping rate of 16 °C/min. Thereafter, the solutions were filtered under vacuum until dry and placed in an oven set to 40 °C overnight to remove excess moisture.

2.5. Preparation of bio-based hybrid supported electrocatalyst

Four Pt electrocatalysts supported on reduced graphene oxide and powdered/granular activated carbon with different rations (1:1 & 1:2), were synthesized using the microwave-assisted modified polyol method. The required amount of chloroplatinic acid (H_2PtCl_6) was dissolved in 15 mL of ethylene glycol ($C_2H_6O_2$), followed by the addition of approximately 400 mg of each hybrid support dissolved in a separate 15 mL of ethylene glycol to achieve a Pt loading of 20 wt%. The ethylene glycol served as both a reducing medium and a dispersant, preventing the agglomeration of hybrid support materials and Pt NPs. About 4 g of NaOH pellets were dissolved in 50 mL ethylene glycol for 18 h to make 2.0 M solution of NaOH. The solution was used to adjust the pH of the catalyst mixture to about 12. The solution beaker was then placed in a microwave reactor at 800 w for 3 min with a maximum temperature of 250 °C. Thereafter the solution underwent reflux and was placed in an oil bath heated at 160 °C for 6 h to increase the reduction of the platinum ions. The

solution was allowed to cool to room temperature then it was placed in a centrifuge at 8000 rpm for 20 min to separate the components. The chloride ions were removed by washing the mixture with de-ionized water and centrifugation at 8000 rpm for 20 min. The four catalysts were placed in an oven set to 70 °C to dry overnight.

2.6. Preparation of stock solution and catalyst ink

The stock solution was prepared by mixing 76.6 mL of de-ionized water with 0.4 mL of 5 % Nafion and 20 mL of isopropanol in a 100 mL volumetric flask. Four catalyst inks were prepared by mixing 10 mg of each Pt hybrid supported catalyst with 5 mL of the stock solution in a vial. The vials were sonicated for 90 min to ensure good dispersion of the Pt hybrid supported catalysts.

2.7. Preparation of testing solutions: 1 M perchloric acid and 1 M methanol

About 43.2 mL of 70 % w/w perchloric acid was added in a 500 mL volumetric flask and filled slowly with de-ionized water to the mark, to prepare 1 M of perchloric acid. The 1 M methanol solution was prepared by adding approximately 20.23 mL of methanol in a 500 mL volumetric flask and filled with de-ionized water to the mark. Both flasks were shaken well and allowed to settle until testing.

2.8. Preparation of the working electrode for testing

To remove any big particles, the surface of the glassy carbon working electrode was first wiped with deionized water and a paper towel. The electrode was then polished in a figure-eight pattern on a polishing pad with a slurry of water and alumina. The polishing process commenced with the 0.3 μm particle size aluminum compound, followed by the utilization of the 0.05 μm particle size aluminum compound. After completing the polishing procedure, the electrode was rinsed with deionized water and left to dry. Once it was completely dry, a volume of 10 μL aliquots of ink was deposited onto the glassy carbon disk and allowed to dry overnight.

2.9. Characterizations

2.9.1. Physicochemical characterization

The crystalline structures of the materials were characterized by Rigaku powder diffractometer with Cu–K α radiation ($\lambda = 1.54$ Å). The diffraction data was collected at 2 θ ranges (5-90°) at a scan rate of 0.01°/min. Fourier transform infrared analysis (FTIR) was recorded in the range (400–4000 cm^{-1}) using a PerkinElmer spectrometer. Raman spectroscopy measurements were performed by Bruker Senterra fitted with a 50 × objective lens for imaging with a 532 nm laser beam, and the spectral data were evaluated using OPUS 7.1 software. The thermal stability of the materials was investigated using Thermogravimetric analysis (TGA) recorded by PerkinElmer, Simultaneous Thermal Analyzer, STA 8000. The studies were conducted at room temperature from 30 °*C* to 800 °*C* at 10 °*C*/min and the cooling was done at 40 °*C*/min. The surface and structure morphology of the obtained materials were carried out on a transmission electron microscope (TEM, JEOL, 2100), and a scanning electron microscope (SEM, TESCAN, VEGA) equipped with a TESCAN dispersive X-ray spectrometer (EDS) with an accelerating voltage of 15 kV. SEM samples were prepared by drop casting on aluminum substrates and dried at 80 °C for 1 h. Similarly, TEM and Raman samples were prepared by drop casting onto copper grids and glass substrates, respectively. University of Cape Town, Electron Microscopic Unit (EMU).

2.9.2. Electrochemical evaluations

The electrochemical investigations were conducted in a conventional three-electrode cell. The as-prepared glassy carbon electrode deposited with the catalyst was used as the working electrode, platinum wire as the counter electrode, and Ag/AgCl (saturated KCl) as the reference electrode. During the electrochemical testing, various techniques such as cyclic voltammetry (CV), methanol oxidation reaction (MOR), electrochemical impedance spectroscopy (EIS), and chronoamperometry were performed on each prepared Pt hybrid supported electrocatalyst. These tests were conducted using an Autolab potentiostat/galvanostat.

To prepare for testing, a 140 mL solution of 1 M perchloric acid was added to the testing beaker. The reference electrode, working electrode, and counter electrode were then placed in the beaker, and nitrogen gas was bubbled through the solution for 30 min. The first test performed was cyclic voltammetry, which involved setting a start potential of −0.300 V, an upper vertex potential of 1.00 V, a lower vertex potential of −0.300 V, a stop potential of −0.200 V, and a scan rate of 0.1 V/s. To warm up the electrode, 40 stop crossings and a scan rate of 0.1 V/s were initially used, followed by the actual test with 1 stop crossing and a scan rate of 0.03 V/s.

For the methanol oxidation reaction (MOR), 60 mL of a 1 M methanol solution was added to the testing beaker, and the solution was bubbled for 30 min. The MOR test utilized a start potential of −0.300 V, an upper vertex potential of 1.00 V, a lower vertex potential of −0.300 V, a scan rate of 0.1 V/s, and 5 stop crossings to warm up the electrode. Then, followed by the actual test with 1 stop crossing and a scan rate of 0.03 V/s. Chronoamperometry followed, utilizing a set potential of 0.58 V with a duration of 3600 s at an interval time of 0.1 s. MOR post chronoamperometry was run immediately after running chronoamperometry using the same MOR settings. Finally, electrochemical impedance spectroscopy was performed using a set potential of 0.58 V.

3. Results and discussion

This section discusses the results obtained from various analytical characterization techniques performed on the synthesized nanomaterials; GO, rGO, rGO/PAC-1:1, rGO/PAC-1:2, rGO/GAC-1:1, rGO/GAC-1:2, Pt-rGO/PAC-1:1, Pt-rGO/PAC-1:2, Pt-rGO/GAC-

1:1 and Pt-rGO/GAC-1:2. The physicochemical characterization of the nanomaterials was performed using X-ray powder diffraction (XRD), Fourier-transform infrared (FTIR) spectroscopy, Raman spectroscopy, Scanning electron microscopy (SEM), Energy dispersive spectroscopy (EDS), and Higher-resolution transmission electron microscopy (HRTEM). The metal loadings were measured by inductively coupled plasma (ICP). Furthermore, electrochemical characterization was performed using cyclic voltammetry, linear sweep voltammetry, electrochemical impedance spectroscopy and chronoamperometry to investigate the catalysts electro-activity.

3.1. XRD patterns

The XRD pattern of graphene oxide (GO) synthesized using modified Hummer's method and thermal conversion to reduce graphene oxide is shown in Fig. 1 below.

The XRD diffraction pattern of GO in Fig. 1 (a) shows diffraction peaks at 2 θ = 10.12 ° and 42.36 °, respectively. The sharp intensive peak at 10.12 ° corresponds to the (001) crystalline planes of GO, which agrees with numerous literature [33,34]. When compared to graphite d-spacing (d_{002} = 0.34 nm), the interlayer distance (d_{001}) calculated using Bragg's law (0.87 nm) shows significant growth. This rise is related to the incorporation of oxygen functional groups into the graphite interlayer, confirming the presence of significant oxidation in the GO structure. Furthermore, a weak diffraction peak located at 42.36 ° is observed due to the partial oxidation of graphite, as shown in Fig. 1 (a).

When GO was reduced to rGO, the (001) peak vanished, and a new broad peak developed at about 24.48 ° with a d-spacing of 0.36 nm, corresponding to the (002) plane, shown in Fig. 1 (b). The broadness of rGO indicates the amorphous structure of rGO. The decrease of d-spacing in rGO from 0.87 nm to 0.36 nm demonstrates complete removal of the oxygen-functional groups (an epoxide group, a carboxylic group, and a hydroxyl group) during the reduction process [34]. The diffraction peak located at 42.36 ° indicates the turbostratic disorder of rGO [35].

Fig. 2 below represents the XRD patterns of (a) rGO, (b) PAC, (c) rGO/PAC-1:1, and (d) rGO/PAC-1:2 synthesized using the hydrothermal method. Fig. 2 shows XRD patterns obtained in the 2 θ range of 0–90° for all materials studied. There is a prominent broad peak at 2 θ = 24.11° in each XRD pattern, which corresponds to the reflection of the (002) plane. This characteristic peak is frequently observed in amorphous structures such as reduced graphene oxide and activated carbon [36,37].

This (002) peak is more noticeable in Fig. 2(a) and (b), however, in Fig. 2 (c), the intensity of this peak decreased due to the hydrothermal process, resulting in the loss of the carbon material's microstructure. However, when the PAC content was raised and mixed with the same mass of rGO, the intensity of the (002) peak increased, indicating a higher degree of turbostratic disorder [38], as shown in Fig. 2 (d). Furthermore, Fig. 2 also shows a weak broad peak at 2 θ = 43.51°, corresponding to the (100) plane, which originates from graphite microcrystalline structures and is influenced by the materials and production procedures utilized [38].

Fig. 3: below shows the XRD patterns of (a) rGO, (b) GAC, (c) rGO/GAC-1:1, and (d) rGO/GAC-1:2 prepared using the hydrothermal method. The XRD pattern of GAC in Fig. 3 (b) showed two common peaks expected in activated carbon material located at 2 θ = 23.99 ° and 2 θ = 43.51 °, and other observed peaks are caused by impurities in GAC. The broad peaks at about 23.99 ° and 43.51 ° in Fig. 3 are attributed to the X-ray reflection in the (002) plane and the (100) plane, which are characteristic to the amorphous structure of

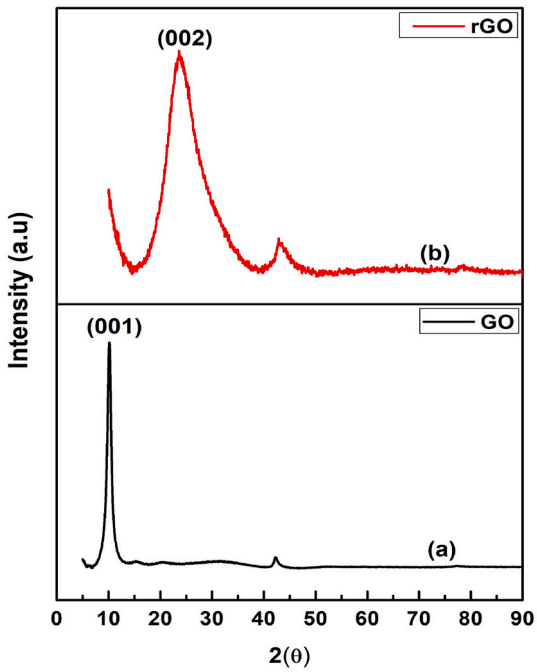

Fig. 1. XRD patterns of (a) GO and (b) rGO.

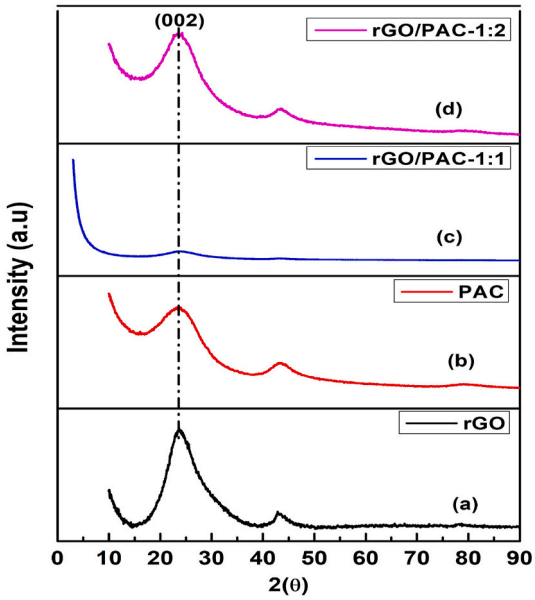

Fig. 2. XRD patterns of (a) rGO, (b) PAC, (c) rGO/PAC-1:1, and (d) rGO/PAC-1:2.

activated carbon [39].

The presence of a sharp and intense peak located at 26.53 ° in Fig. 3(b and c & d) implies the existence of graphite crystallite in GAC [40]. The introduction of rGO in GAC-1:1 and 1:2 increased the broadness and intensity of plane (002), which indicates that rGO has been successfully incorporated in GAC. Hence, a more amorphous carbon composite has been achieved. To evaluate whether Pt nanoparticles are well deposited on hybrid supports, Pt electrocatalysts were characterized with XRD. The XRD patterns of (a) Pt-rGO/PAC-1:1, (b) Pt-rGO/PAC-1:2, (c) Pt-rGO/GAC-1:1, and (d) Pt-rGO/GAC-1:2 electrocatalysts are shown in Fig. 4 below:

Fig. 4 above represents the successful deposition of Pt nanoparticles on the hybridized rGO/PAC and rGO/GAC, it can be observed

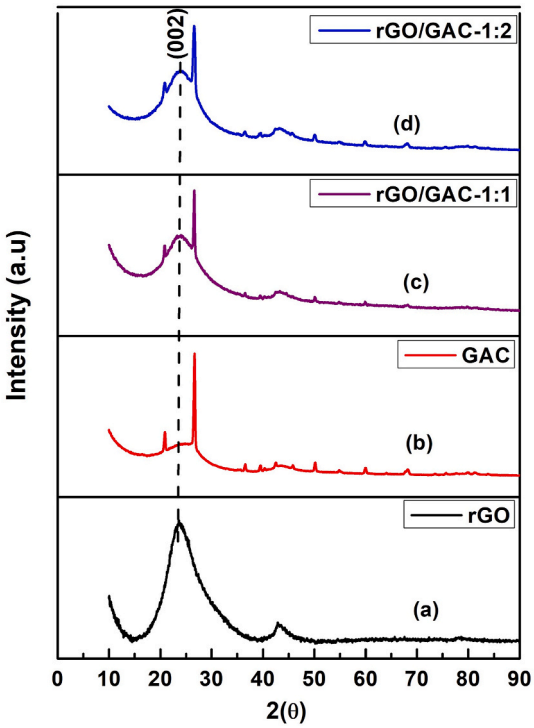

Fig. 3. XRD patterns of (a) rGO, (b) GAC, (c) rGO/GAC-1:1, and (d) rGO/GAC-1:2.

that all the XRD patterns have a broad peak at 2 $\theta = 25.84^\circ$ of plane (002) attributed to the presence of amorphous carbon [41]. This plane (002) was also observed in Fig. 1(b)–s. 2 and 3 of the hybrids. In Fig. 4, broad diffraction peaks located at 2 $\theta = 40.84$, 46.10, 68.90, and 81.99 ° representing the (111), (200), and (220) planes are observed, respectively. These peaks matched the face-centered cubic (fcc) crystal structure of platinum (Pt) as listed in the (JCPDS Card 04-0802), providing clear evidence of the presence of crystalline Pt nanoparticles [34,42]. However, most of the Pt diffraction peaks are observed in Fig. 4 (b), suggesting more crystalline material compared to Fig. 4(a)–(c), and (d). Even so, the weak and broad peaks in Fig. 4(a)–(c), and (d) still suggest the presence of Pt nanoparticles on them. The average crystallographic size of Pt particles is determined using the Debye-Scherrer equation (see Equation (4)) from the full width of the half maximum (FWHM) of the most intense peak (111) [42].

$$D = \frac{0.9\lambda}{\beta \cos\theta} \tag{4}$$

where d is the average size (nm), k is the constant depending on the crystallite shape (0.9), λ is the wavelength of copper Kα X-ray radiation (0.154 nm), β is the FWHM calculated from the (111) peak by using Originlab software (in radians), and θ is the diffraction angle. The obtained results show that the Pt-rGO/PAC-1:1, Pt-rGO/PAC-1:2, Pt-rGO/GAC-1:1 and Pt-rGO/GAC-1:2 electrocatalysts exhibit crystalline size of about 1.36 nm, 1.68 nm, 1.40 nm, respectively.

3.2. FTIR spectroscopy

Fig. 5 below represents the FTIR spectra of graphene oxide (GO) and reduced graphene oxide (rGO). Fig. 5 above shows the FTIR spectra of GO (black) prepared using modified Hummer's method and its thermal conversion to rGO (red). The GO spectrum shows a broad signal located at 3322 cm^{-1} attributed to the stretching vibration of hydroxyl groups formed from absorbed water molecules, phenols or OH from carboxylic groups. The peak at around 1723 cm^{-1}corresponds to the C═O stretching vibration of the carboxyl group, 1394 cm^{-1} is attributed to the C–OH stretch of alcohol group, and 1025 cm^{-1} is due to the C–O stretching vibrations of the epoxy groups [43,44].

FT-IR spectroscopy was also used to analyse the reduction of GO. Fig. 5 illustrates that the peaks representing oxygen-containing functional groups in rGO exhibited reduced intensities compared to those in GO, and some peaks even vanished (C–OH). Hence, these FTIR spectra indicate the successful reduction of GO through thermal conversion.

Fig. 6 shows the FTIR spectra of (a) granular activated carbon (GAC) and (b) powdered activated carbon (PAC) derived from macadamia nut shells. These activated carbon materials were used as one part of the catalyst support. The FTIR spectrum of GAC derived from macadamia nutshell is shown in Fig. 6 (a). The broad band observed at 3706 cm^{-1} corresponds to the vibrational stretching of the hydroxyl functional group, possibly due to the absorbed water used in the preparation procedure [45]. The shoulder band situated at 2907 cm^{-1} is attributed to the aliphatic C–H stretch of CH, CH_2 and CH_3 groups [46], while the band at 2127 cm^{-1} corresponds to the stretching vibrations of –C ≡ C- of alkynes [47,48].

The very weak band at 1527 cm^{-1} can be attributed to the C–O vibrational stretching of a carboxylic group [48]. The peak at 1091 can be assigned to C–OH stretching of phenolic groups [49]. An out of plane band in aromatic compounds is observed at 784 cm^{-1}

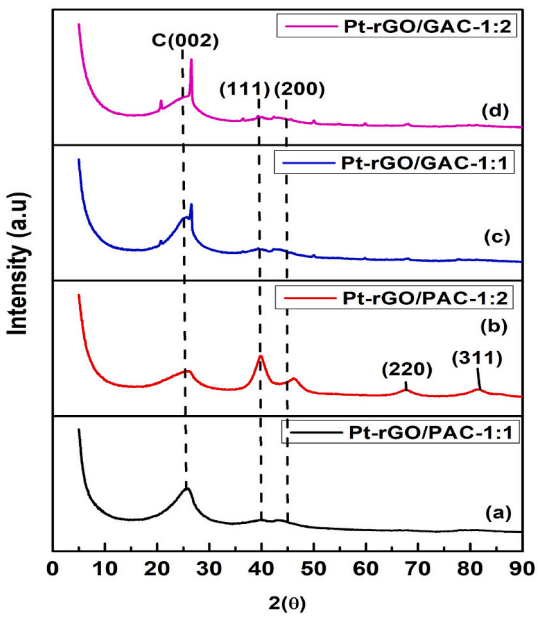

Fig. 4. XRD patterns of (a) Pt-rGO/PAC-1:1, (b) Pt-rGO/PAC-1:2, (c) Pt-rGO/GAC-1:1 and (d) Pt-rGO/GAC-1:2 electrocatalysts.

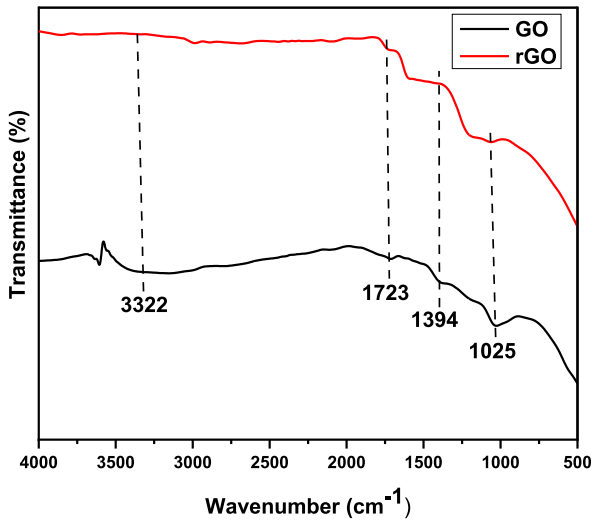

Fig. 5. FTIR spectra of GO (black) and rGO (red). (For interpretation of the references to colour in this figure legend, the reader is referred to the Web version of this article.)

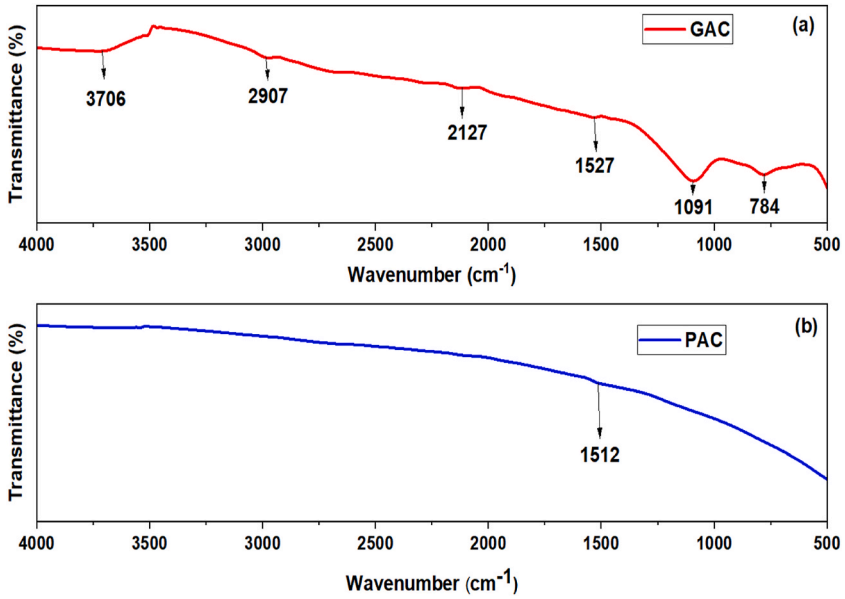

Fig. 6. FTIR spectra of (a) granular activated carbon (GAC) and (b) powdered activated carbon (PAC) derived from macadamia nut shells.

corresponding to C–H stretching vibration [50]. Fig. 6 (b) shows a band at 1512 cm^{-1} corresponding to the stretching vibration of the C–C bond [51].

Fig. 7 below represents the FTIR spectra of (a) reduced graphene oxide (rGO), (b) reduced graphene oxide/powdered activated carbon (1:1), and (c) reduced graphene oxide/powdered activated carbon (1:2).

In Fig. 7, functional groups in the hybrid supports resemble those found in rGO, indicating a successful composite formation between rGO and all ratios of PAC. The weak vibrational band at 1727 cm^{-1} in Fig. 7(a–c) is attributed to the C═O carbonyl stretching, and bands located at 1197 cm^{-1} and 1036 cm^{-1} are due to C–O epoxide group stretching and C–O–C vibrational stretching, respectively [52,53]. These identified functional groups in Fig. 7(b) and (c) provide further confirmation of the formation of composites between rGO and PAC at different ratios.

Fig. 8 below shows the FTIR spectra of (a) reduced graphene oxide (rGO), (b) reduced graphene oxide/granular activated carbon (1:1), and (c) reduced graphene oxide/granular activated carbon (1:2).

The hybrid supports in Fig. 8(b) and (c) consist of functional groups found in rGO and GAC in Figs. 6 (a) and 8 (a). Some of the functional groups that were present in Fig. 6 (a) are no longer visible in all ratios of the hybrid supports. Functional groups such as the

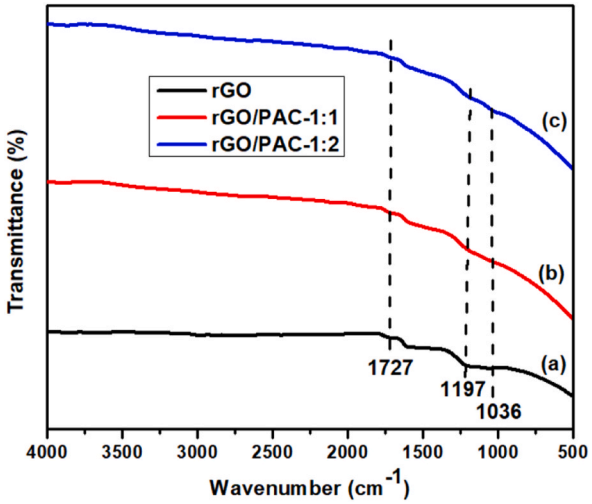

Fig. 7. FTIR spectra of (a) rGO (black), (b) rGO/PAC-1:1 (red) and (c) rGO/PAC-1:2 (blue) hybrid supports. (For interpretation of the references to colour in this figure legend, the reader is referred to the Web version of this article.)

hydroxyl group, alkynes, and carboxylic group vibrational stretching were removed during the hydrothermal process when forming the hybrid supports. The band located at 2941 cm^{-1} is caused by the aliphatic C–H stretch of CH, CH_2 and CH_3 group, this vibrational stretching is also shown in Fig. 6 (a). The peaks found at 1732 cm^{-1} and 1041 cm^{-1} in Fig. 8(a–c) are due to C═O carbonyl stretching vibration and C–O stretching of the epoxy group, respectively [53]. The presence of these functional groups in rGO and GAC confirms the formation of the hybrid supports in all ratios.

Fig. 9 below represents the FTIR spectra of (a) Pt-rGO/PAC-1:1 and Pt-rGO/PAC-1:2 electrocatalysts.

The weak vibrational bands observed in Fig. 9(a) and (b) above correspond to the functional groups discussed in Fig. 7(b) and (c). However, in Fig. 9(a) and (b), these vibrational bands are observed at both lower and higher wavenumbers due to the presence of Pt nanoparticles. Specifically, the C═O carbonyl stretching, which was previously observed at 1727 cm^{-1} in Fig. 7(a–c), has now shifted to a lower wavenumber of 1612 cm^{-1} [34]. Furthermore, a C–OH vibrational peak is observed at wavenumber 1214 cm^{-1} [54]. This peak was not observed in the hybrid supports in Fig. 7(b) and (c), but it becomes apparent after the incorporation of Pt onto the hybrid supports.

Fig. 10 below shows the FTIR spectra of (a) Pt-rGO/GAC-1:1 and Pt-rGO/GAC-1:2 electrocatalysts.

The successful incorporation of Pt nanoparticles onto the hybrid supports (rGO/GAC-1:1 and rGO/GAC-1:2) can be supported by the absence and change of functional group positions in Fig. 10(a) and (b). In Fig. 8(b) and (c), an aliphatic C–H peak at 2941 cm^{-1}, a C═O carbonyl band at 1732 cm^{-1}, and a C–O stretching of the epoxy group at 1041 cm^{-1} were observed. However, upon introducing Pt onto the hybrid supports, notable changes occurred. The C–H peak diminished, and the position of the C═O band shifted from 1732

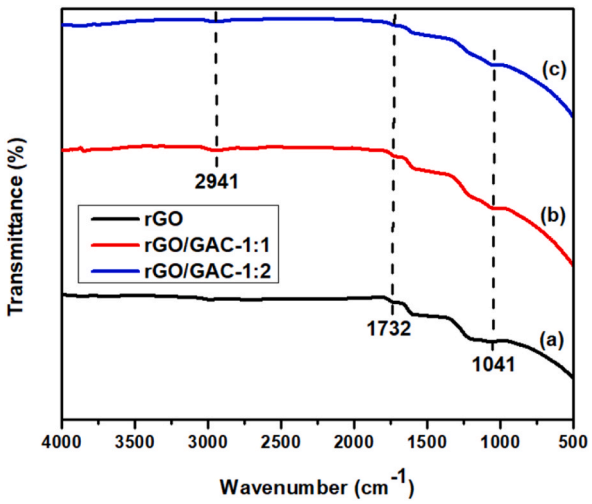

Fig. 8. FTIR spectra of (a) rGO (black), (b) rGO/GAC-1:1 (red) and (c) rGO/GAC-1:2 (blue) hybrid supports. (For interpretation of the references to colour in this figure legend, the reader is referred to the Web version of this article.)

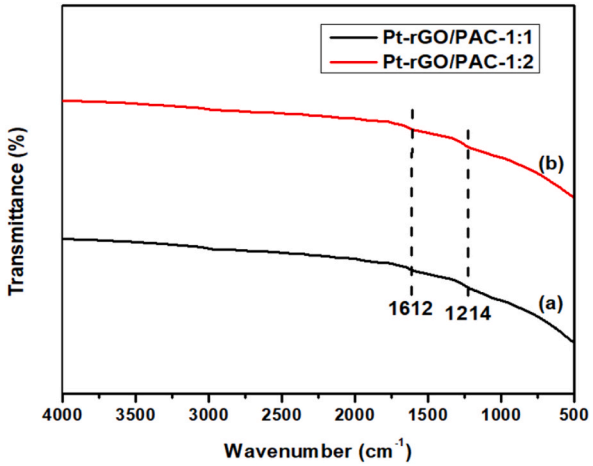

Fig. 9. FTIR spectra of (a) Pt-rGO/PAC-1:1 and Pt-rGO/PAC-1:2 electrocatalysts.

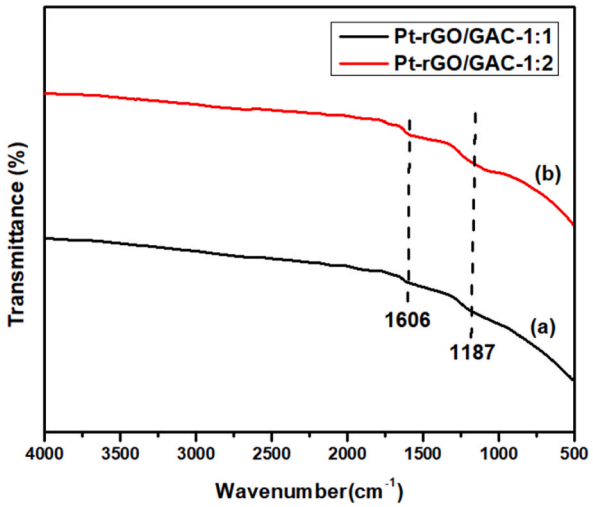

Fig. 10. FTIR spectra of (a) Pt-rGO/GAC-1:1 and Pt-rGO/GAC-1:2 electrocatalysts.

cm^{-1} to 1606 cm^{-1}, while the epoxy group moved to a higher wavenumber of 1187 cm^{-1}, as shown in Fig. 10(a) and (b). These observed changes in functional group positions provide strong evidence supporting the successful incorporation of Pt nanoparticles.

3.3. Raman spectroscopy

Raman spectroscopy was used to determine the degree of defect and disorder in the as-synthesized materials, Fig. 11 below.

Three prominent peaks corresponding to the D, G, and 2D bands are observed in Fig. 11 above. The broad Raman signal at 1356 cm^{-1} for GO and rGO is due to the sp^3 (D-band) defects in the structure of GO, while the signal at 1583 cm^{-1} attributed to the G-band is due to the E_{2g} vibration of sp^2 in GO and rGO [55]. In GO, the 2D-band at 2908 cm^{-1} indicates the development of the graphene structure [56], confirming that the produced GO is multilayered since monolayer graphene typically exhibits a peak at 2679 cm^{-1} [57]. The absence of the 2D band in rGO confirms the removal of oxygen-containing functional groups. The I_D/I_G ratio for GO and rGO was calculated to be 0.75 and 0.81, respectively. The increase in the I_D/I_G for rGO is caused by the restoration of sp^2 and the decrease in the average sizes of sp^2 during the reduction process [57].

Fig. 12 represents the Raman spectra of (a) rGO, (b) PAC, (c) rGO/PAC-1:1, and (d) rGO/PAC-1:2. The Raman spectra of the composites are shown in Fig. 12, and a broad D band and a strong G band of the first-order are observed at the Raman shift of 1352 cm^{-1} and 1592 cm^{-1} respectively, for all composites. The broadness of the D-band (sp^3 hybridized) in Fig. 12 indicates the presence of defects or impurities in the composites [58]. However, the strong intensity of the G-band indicates the presence of numerous sp^2 hybridisations between carbon atoms. The staking order of PAC, rGO/PAC-1:1, and rGO/PAC-1:2 in Fig. 12 is attributed by the presence of the 2D band located at 2815, 2702 and 2814 cm^{-1}, respectively. The appearance of this band confirms the successful

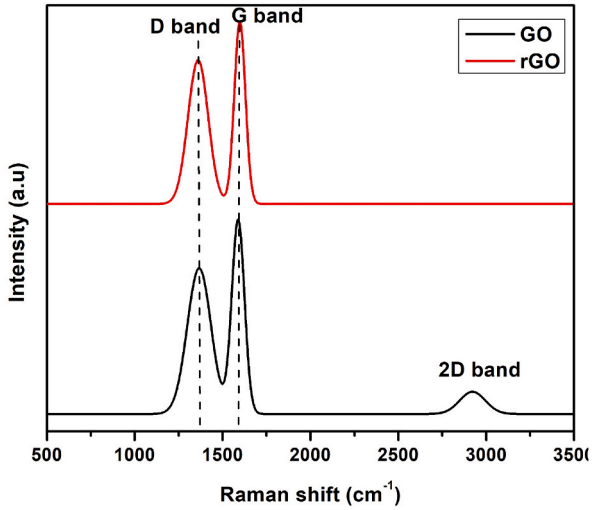

Fig. 11. Raman spectra of GO and rGO.

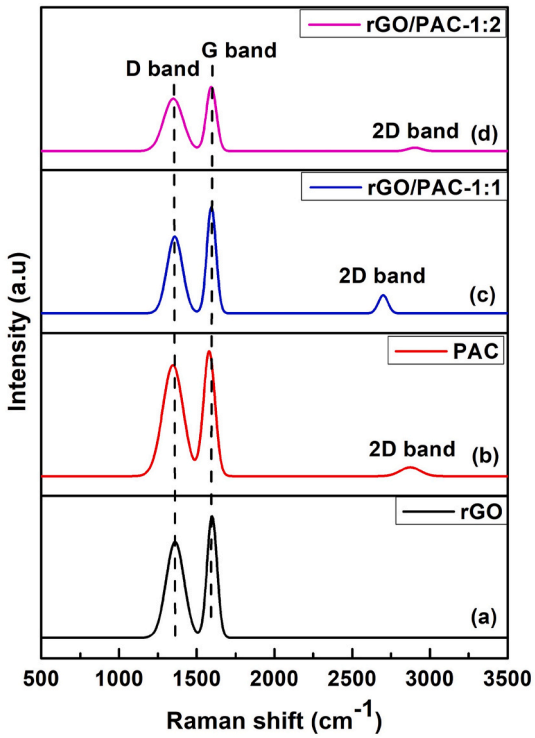

Fig. 12. Raman spectra of (a) rGO, (b) PAC, (c) rGO/PAC-1:1 and (d) rGO/PAC-1:2.

formation of the composites since it was absent in rGO but became evident after introducing PAC, as observed in Fig. 12(c) and (d). As the 2D band is positioned above 2700 cm^{-1}, it indicates that the composites are multilayered, in line with existing literature [59].

The ratios of the intensities of the D band and the G band (I_D/I_G) for rGO, PAC, rGO/PAC-1:1 and rGO/PAC-1:2 are 0.81, 0.92, 0.85, and 0.88, respectively. The D-band to G-band ratio is a crucial indicator for determining the extent of defects in carbon samples. The increase in the ratio from 0.81 (rGO) to 0.85 (rGO/PAC-1:1) and 0.88 (rGO/PAC-1:2) indicated that more defects were formed during the hydrothermal process [60].

The Raman spectra of (a) rGO, (b) GAC, (c) rGO/GAC-1:1 and (d) rGO/GAC-1:2 electrocatalysts are shown in Fig. 13 below. Fig. 13 above represents the Raman spectra of rGO, GAC, rGO/GAC-1:1, and rGO/GAC-1:2, it is observed that all the investigated samples show two characteristic D and G bands of rGO. The D and G bands of rGO and GAC were identified at 1361 and 1337 cm^{-1}, and 1592

and 1600 cm^{-1}, respectively. Additionally, the peaks observed at 1368 cm^{-1}, 1365 cm^{-1}, 1582 $cm^{-1}$and 1580 cm^{-1} are due to the D and G bands of rGO/GAC-1:1 and (d) rGO/GAC-1:2 after sintering, respectively. The presence of the D band in all the samples implies the existence of carbon structures with defects or disorders, while the G band signifies the presence of ordered graphitic structures containing sp^2-hybridized carbon atoms [61,62].

The broadness of the D band signifies the amorphous structure of the samples in Fig. 13(a–d). Moreover, GAC demonstrates a higher D band intensity compared to rGO, rGO/GAC-1:1, rGO/GAC-1:2, and PAC (see Fig. 12 (b)), suggesting that it is more amorphous than PAC in Fig. 12 (b). The intensity of the G band is slightly higher than that of the D band, indicating that the composites possess crystalline, ordered, and defect structures within the carbon lattice [61]. The weak 2D bands located at 2853, 2909 and 2910 cm^{-1} corresponding to GAC, rGO/GAC-1:1 and rGO/GAC-1:2 respectively, indicate the presence of multilayered structures [59]. The intensity ratios of the D and G band (I_D/I_G) for rGO, GAC, rGO/GAC-1:1 and rGO/GAC-1:2 are 0.81, 1.03, 0.83, and 0.88, respectively. The increase in the I_D/I_G ratio suggested that more defects were created during the incorporation of GAC into rGO.

Raman spectroscopy was used to examine the degree of graphitization and structural characteristics of Pt-rGO/PAC-1:1, Pt-rGO/PAC-1:2, Pt-rGO/GAC-1:1, and Pt-rGO/GAC-1:2, as shown in Fig. 14(a–d), respectively. All the electrocatalysts in Fig. 14(a–d) had the same Raman peak positions for the D (1344 cm^{-1}) and G (1584 cm^{-1}) bands. The changes in the position of the D band, from 1352 to 1365 cm^{-1} (see Figs. 12 and 13) to 1344 cm^{-1} in Fig. 13, and also the G band, from 1592 to 1584 cm^{-1} (see Figs. 12 and 13) to 1584 cm^{-1} in Fig. 13 are due to the introduction of Pt nanoparticles on the carbon hybrids. The D band is a characteristic feature of the sp^3 hybridized carbon, which results from defects in carbon materials, while the G band represents the E_{2g} vibration of sp^2 bonds between carbon atoms [63].

The weak 2D bands located at 2886 cm^{-1},2861 cm^{-1}, 2909 cm^{-1} and 2902 cm^{-1} as shown in Fig. 14(a–d), respectively, suggest the attachment of Pt nanoparticles to a multilayered carbon structure [64]. Additionally, the intensity of the D and G bands (I_D/I_G) in the Raman spectrum can be used to scrutinize the extent of defects in the carbonaceous material. The I_D/I_G values were found to be 0.81, 0.85, 0.76, and 1.00 for Pt-rGO/PAC-1:1, Pt-rGO/PAC-1:2, Pt-rGO/GAC-1:1, and Pt-rGO/GAC-1:2, respectively. All metal-deposited hybrid samples exhibit a higher I_D/I_G ratio than GO, which implies the restoration of sp^2 domains during reduction and the interaction between the different carbon structures during the preparation process. Consequently, the introduction of PAC and GAC onto the rGO stimulates the surface structure of the material, potentially improving the redox activities [65].

3.4. TGA analysis

Fig. 15 below represents the TGA curves of (a) GO and (b) rGO under N_2 atmosphere.

In Fig. 15 (a), the slight weight loss (~5 %) below 100 °C is attributed to the evaporation of water molecules from the surface of GO. The significant weight loss (~60 %) within the temperature range of 180–184 °C is due to the elimination of epoxy, hydroxyl, and

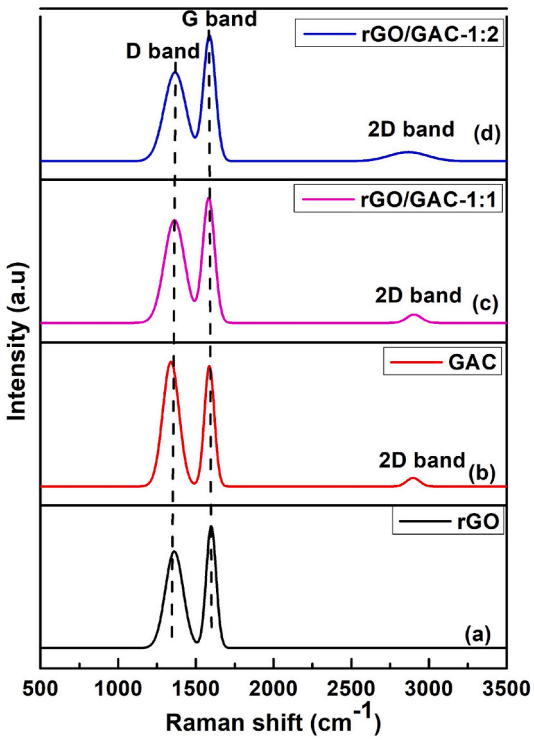

Fig. 13. Raman spectra of a) rGO, (b) GAC, (c) rGO/GAC-1:1 and (d) rGO/GAC-1:2.

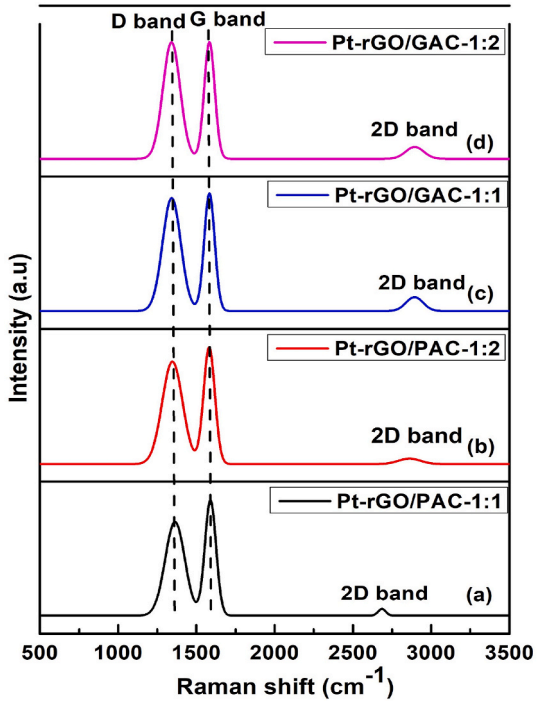

Fig. 14. Raman spectra of (a) Pt-rGO/PAC-1:1, (b) Pt-rGO/PAC-1:2, (c) Pt-rGO/GAC-1:1, and (d) Pt-rGO/GAC-1:2.

residual water molecules. The complete breakdown of carbon occurs within the temperature range of 250–500 °C [66,67]. Compared to GO, rGO in Fig. 15 (b) has better thermal stability below 184 °C and complete decomposition near 700 °C. The improved thermal stability of rGO is a result of graphitization and the reinforcement of van der Waals forces between layers achieved by the removal of oxygen functional groups [66]. The unstable state of rGO is because the tested samples are very light in weight.

The TGA curves of (a) rGO, (b) rGO/PAC-1:1, (c) PAC, and (d) rGO/PAC-1:2 investigated under N_2 atmosphere are shown in Fig. 16.

The successful incorporation of rGO with PAC is also revealed in TGA curves in Fig. 16 (b) & (d). The sudden drop in weight of about 15 % at temperatures below 200 °C for PAC is attributed to the loss of moisture in the material [68], and from 249 to 500 °C the complete breakdown of carbon and devolatilization of organic matter occurred. All the hybrids support, Fig. 16 (b) and (d) exhibit two stages of decomposition. The first stage with a weight loss of about 5 % occurred below 100 °C and is due to the evaporation of water. The last stage is the complete decomposition of carbon in the range 249–790 °C. Although rGO/PAC-1:1 and rGO/PAC-1:2 show the same stages of decomposition, rGO/PAC-1:1 has a higher weight loss than rGO/PAC-1:2. Hence, rGO/PAC-1:2 has a higher thermal

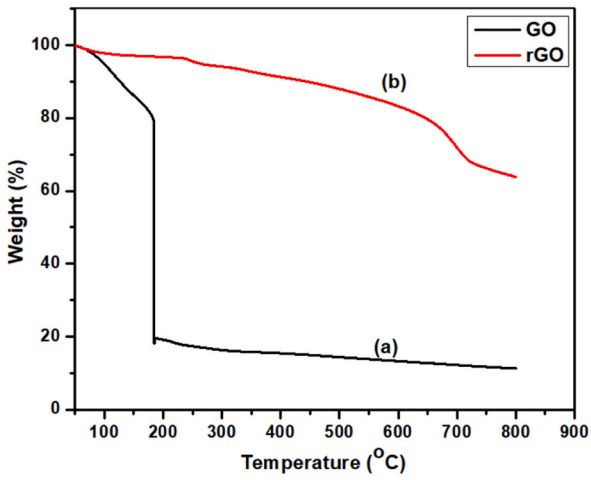

Fig. 15. TGA curves of (a) GO and (b) rGO under N_2 atmosphere.

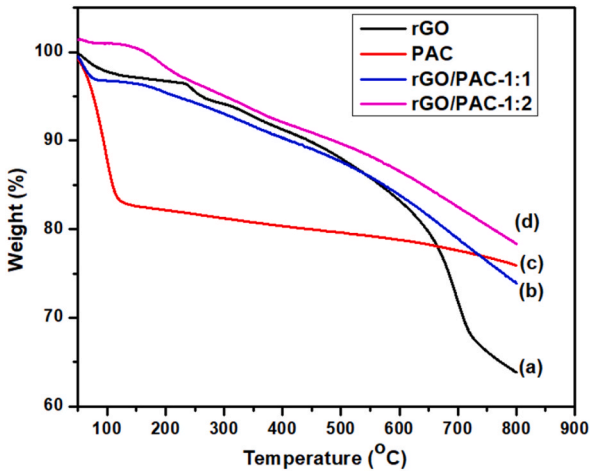

Fig. 16. TGA curves of (a) rGO, (b) rGO/PAC-1:1, (c) PAC, and (d) rGO/PAC-1:2 under N_2 atmosphere.

stability than rGO/PAC-1:1.

Fig. 17 below represents the TGA curves for (a) rGO, (b) rGO/GAC-1:1, (c) rGO/GAC-1:2, and (d) GAC under N_2 atmosphere.

The TGA curve of GAC in Fig. 17 (d) shows two stages of decomposition in the ranges of 0–100 °C and 294-700 °C, respectively. The first weight loss of about 6 % at the temperature range of 0–100 °C is caused by the loss of water molecules in the material. The second decomposition stage from 294 to 700 °C is a result of the devolatilization of organic matter and degradation of surface functional groups [69]. Both, rGO/GAC-1:1 and rGO/GAC-1:2 in Fig. 17(b) and (c) exhibit a weight loss of approximately 3 % and 6 % below 100 °C, this weight loss is due to the evaporation of water molecules from the surface. The last decomposition stage in rGO/GAC-1:1 and rGO/GAC-1:2 in the temperature range 294–700 °C is attributed to the degradation of hemicellulose, cellulose, lignin, and carbon skeleton. The increase in weight loss from 700 to 800 °C indicates the presence of carbonyls in the hybrids [70]. Fig. 17 (c) also shows that rGO/GAC-1:2 is more thermally stable than rGO/GAC-1:1 due to its slight drop in weight (%).

Fig. 18 represents TGA analysis of (a) Pt-rGO/PAC-1:1, (b) Pt-rGO/PAC-1:2, (c) Pt-rGO/GAC-1:1 and (d) Pt-rGO/GAC-1:2 electrocatalysts under N_2 atmosphere.

The initial weight loss displayed in Fig. 18(a–d), observed across all electrocatalysts within the 0-200 °C temperature range, can be attributed to the evaporation of moisture from the carbon hybrid supports. The introduction of Pt nanoparticles on the rGO/PAC-1:1, rGO/PAC-1:2, rGO/GAC-1:1, and rGO/GAC-1:2 support in Fig. 18(a–d) lowered the oxidation temperature to about 520 °C suggesting a catalytic process where the Pt NPs facilitates the oxidation of carbon hybrids at low temperatures [71]. Fig. 18 (d) further illustrates that Pt-rGO/GAC-1:2 exhibits greater thermal stability, followed by Pt-rGO/GAC-1:1, Pt-rGO/PAC-1:2, and finally Pt-rGO/PAC-1:1.

3.5. SEM-EDS micrographs

SEM was used to evaluate the morphologies of GO, rGO, rGO/PAC-1:1, rGO/PAC-1:2, rGO/GAC-1:1, rGO/GAC-1:2, Pt-rGO/PAC-

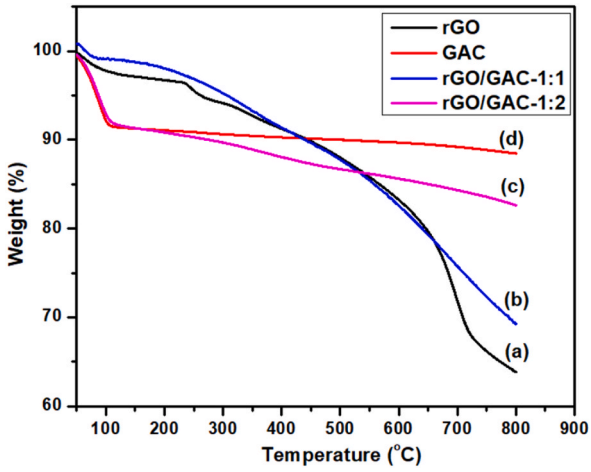

Fig. 17. TGA curves of (a) rGO, (b) rGO/GAC-1:1, (c) rGO/GAC-1:2, and (d) GAC under N_2 under N_2 atmosphere.

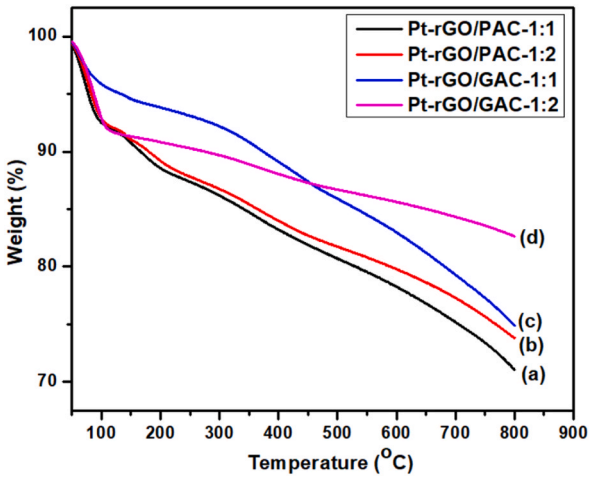

Fig. 18. TGA curves of (a) Pt-rGO/PAC-1:1, (b) Pt-rGO/PAC-1:2, (c) Pt-rGO/GAC-1:1 and (d) Pt-rGO/GAC-1:2 electrocatalysts under N_2 atmosphere.

1:1, Pt-rGO/PAC-1:2, Pt-rGO/GAC-1:1, and Pt-rGO/GAC-1:2 samples. Fig. 19 shows the SEM-EDS micrographs for (a & b) GO and (c & d) rGO at different magnifications. The surface of GO in Fig. 19(a) and (b) shows crumpled, wrinkled, and layered flakes held together by strong π-π interactions [72]. Individual sheets can be distinguished by their edges, which are wrinkled. The crumpling, wrinkles, and rough surface of the GO are due to structural deformation during exfoliation and restacking of the sheets [73]. These sheets consist of multilayers of GO platelets, which is also supported by Raman results. Hidayah et al. reported a similar type of morphology [74]. The SEM images of rGO in Fig. 19(c) and (d) reveal overlapped and shredded sheets that lead to curtain-like sheets with zig-zig edges [73]. This overlapping of the sheets indicates a multilayered structure, which also corresponds to the Raman results.

The presence of carbon, oxygen, sulfur, and potassium in the EDS spectrum of GO in Fig. 19 indicates the successful synthesis of GO using the modified Hummers' method. The EDS spectrum of rGO, as shown in Fig. 19 (f), also confirms the presence of carbon, oxygen, potassium, and sodium. However, these elements have been reduced in quantity due to the thermal reduction of GO, which led to the successful production of rGO. Also, the decreased amount of oxygen molecules in rGO and the increased carbon content confirm the successful reduction of GO to rGO.

Fig. 20 represents the SEM-EDS micrographs at different magnifications for (a & b) PAC, (c & d) rGO/PAC-1:1, and (e & f) rGO/PAC-1:2.

The SEM image shown in Fig. 20 (a) revealed that the PAC particles have a partially smooth surface with irregular shapes and different pore types, typical of activated carbon with a high surface area [75]. In Fig. 20 (c & e), the rGO/PAC-1:1 and rGO/PAC-1:2 composites show larger and layered sheets with comparative agglomeration. The rGO sheets in Fig. 20 (c) are restacked due to the addition of a smaller amount of PAC, which was introduced to hinder the restacking process, as described by Wang et al. [76]. In contrast, the rGO/PAC-1:2 composite in Fig. 20 (e) is slightly expanded with PAC between the rGO sheets, suggesting that the PACs in the composite were coated with wavy and wrinkled rGO sheets layer by layer. This also, indicates that PAC acted as a binder between rGO sheets to prevent re-stacking and provided a conductive bridge for ion transport [77].

The wavy, crumpled sheets observed in Fig. 20 (c & e) are due to the presence of rGO [78], which indicate the successful formation of the composite between rGO and PAC. The carbon content in Fig. 20 (d) and (f) has increased by 1.07 % for rGO/PAC-1:1 and 6.8 % for rGO/PAC-1:2 when compared to the content in Fig. 19 (f) due to the presence of PAC. Also, the hydrothermal reaction employed in the composite preparation has led to a decrease in oxygen, sulfur, and potassium content originally present in the rGO, as shown in Fig. 19 (f).

Fig. 21 below shows the SEM-EDS micrographs at different magnifications for (a & b) GAC, (c & d) rGO/GAC-1:1, and (e & f) rGO/GAC-1:2.

The morphology displayed in Fig. 21 (a) revealed that GAC has a rough surface texture with pores, which is common in activated carbon with a high surface area [75]. Furthermore, the surface of the carbon has random pieces of white blocks with different sizes and forms. The EDS spectra depicted in Fig. 21 (b) show that these small white blocks consist of materials containing silicon, along with other elements like aluminum and sulfur, potentially significant for plants. In Fig. 21 (c), the rGO sheets are clearly visible within the rGO/GAC-1:1 composite, due to the low GAC content used in composite formation. This indicates that the rGO sheets coated the GAC surface, which corresponds with the results reported in previous studies [62]. The physical morphology of rGO/GAC-1:2 displayed in Fig. 21 (e), shows a rough surface with wrinkles on the composite's surface. These wrinkles signify the presence of rGO within the composite. The increase in the content of GAC has resulted in the full coating of the rGO sheets, as shown in Fig. 21 (e). Furthermore, the addition of GAC to rGO has resulted in a decrease in the carbon content by 4.14 % and 2.65 % for rGO/GAC-1:1 and rGO/GAC-1:2, respectively, as shown in Fig. 21 (d & f). This decline in carbon content is due to an increase in the presence of oxygen molecules as a result of chemical interactions between rGO and GAC.

Fig. 22 shows SEM-EDS micrographs of electrocatalysts at various magnifications for (a & b) Pt-rGO/PAC-1:1, (c & d) Pt-rGO/PAC-

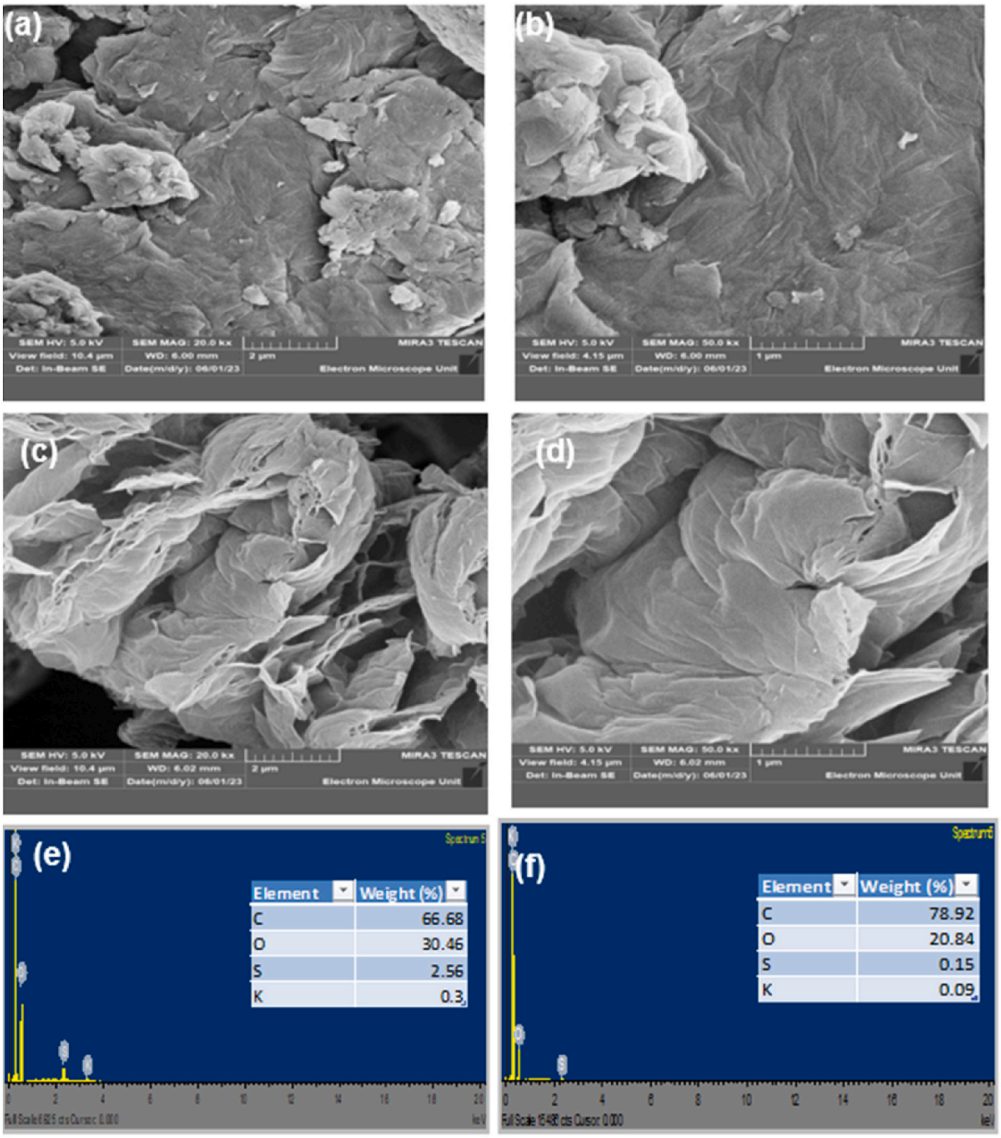

Fig. 19. SEM images of (a & b) GO and (c & d) rGO at different magnifications, and EDS spectra of (e) GO and (f) rGO.

1:2, (e & f) Pt-rGO/GAC-1:1, and (g & h) Pt-rGO/GAC-1:2.

The SEM images of the electrocatalysts displayed in Fig. 22(a–c, e & g) have a smooth surface with non-uniform and spherically shaped Pt nanoparticles. The distribution of Pt nanoparticles on the surfaces of rGO/PAC-1:1, rGO/PAC-1:2, rGO/GAC-1:1 and rGO/GAC-1:2 was achieved after the proposed microwave polyol method. Fig. 22 (c) shows agglomerated Pt NPs, while in Fig. 22(a–e & g), the Pt NPs are scattered over the hybrid surface. The bright tiny spots were confirmed to be Pt nanoparticles by EDS analysis, as shown in Fig. 22(b–d, f & h).

3.6. HRTEM analysis

High resolution transmission electron microscope (HRTEM) was used to examine the internal structure and distribution of Pt nanoparticles of the produced hybrid supports and catalysts. Fig. 23 represents the HRTEM images of (a) GAC, (b) PAC, (c) rGO, (d) rGO/PAC-1:1, (e) rGO/PAC-1:2, (f) rGO/GAC-1:1 and (g) rGO/GAC-1:2 at different magnifications.

Fig. 23(a) and (b) displays HRTEM images of GAC and PAC, respectively, with lighter coloring in the pore region due to the electron beam passing through them, whereas the pore walls appear darkened due to electron scattering [79]. A smooth and layered structure with a wrinkled surface representing rGO is observed in Fig. 23 (c) [80], which is consistent with previous observations made using SEM in Fig. 23 (c and d). The HRTEM image of rGO/PAC-1:1 in Fig. 23 (d) reveals the presence of wrinkled rGO covered by porous PAC. However, in Fig. 23 (e), no visible flakes of rGO are seen, this might be due to the increased carbon content of PAC. Fig. 23 (f)

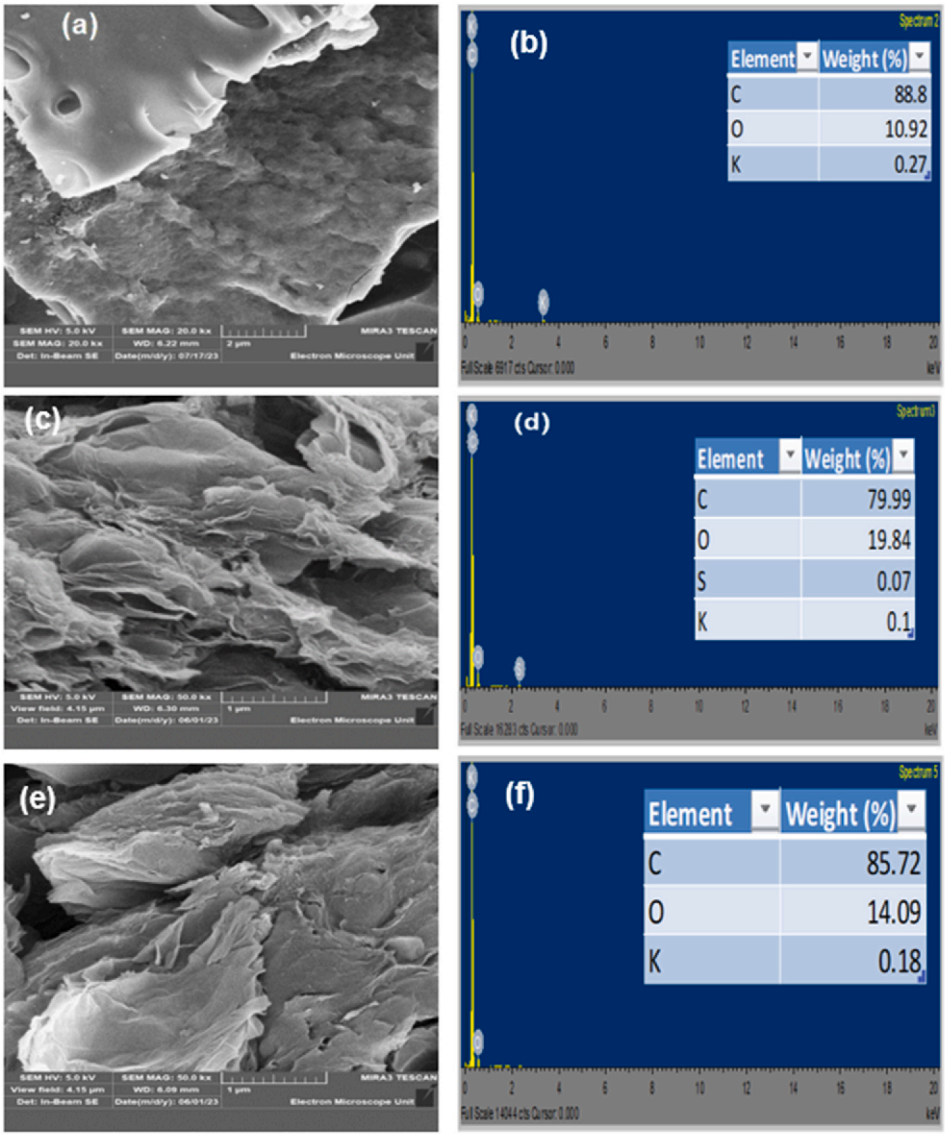

Fig. 20. SEM-EDS micrographs at different magnifications for (a & b) PAC, (c & d) rGO/PAC-1:1, and (e & f) rGO/PAC-1:2.

shows aggregated rGO/GAC-1:1 hybrid sheets with spots of hollow spheres. Whereas Fig. 23 (g) displays irregularly structured sheets with partial aggregation. The presence of pores in Fig. 23(d, e, f &g) suggests that PAC and GAC are evenly distributed on the RGO sheets, thus three-dimensional porous hybrids were achieved [81].

Fig. 24 below shows the Pt nanoparticles distribution by HRTEM images of (a) Pt-rGO/PAC-1:1, (b) Pt-rGO/PAC-1:2, (c) Pt-rGO/GAC-1:1, (d) Pt-rGO/GAC-1:2 at 20 nm magnification, and corresponding size histograms of (e) Pt-rGO/PAC-1:1, (b) Pt-rGO/PAC-1:2, (c) Pt-rGO/GAC-1:1, and (d) Pt-rGO/GAC-1:2.

Fig. 24(a–d) shows the 2D planar sheet feature of reduced graphene oxide (rGO), which is combined with powdered activated carbon (PAC) and granular activated carbon (GAC) for all electrocatalysts. Spherical platinum (Pt) nanoparticles (depicted as dark dots) are dispersed across the hybrid supports of rGO/PACs and rGO/GACs. Compared to other electrocatalysts, Pt-rGO/PAC-1:2 in Fig. 24 (b) exhibits the least aggregation, followed by Pt-rGO/GAC-1:2 (Fig. 24 (d)), Pt-rGO/PAC-1:1 (Fig. 24 (a)), and Pt-rGO/GAC-1:1 (Fig. 24 (c)). This feature is desired for good catalyst performance and durability of Pt electrocatalysts [82,83]. Fig. 24 (c) shows less distribution of Pt nanoparticles on the surface of rGO/GAC-1:1, potentially due to either the image being magnified at a lower level or insufficient attachment of Pt nanoparticles to the hybrid support's surface. The average particle size of Pt-rGO/PAC-1:1, Pt-rGO/PAC-1:2, Pt-rGO/GAC-1:1 and Pt-rGO/GAC-1:2 electrocatalysts were found to be 2.10 nm, 2.10 nm, 1.91 nm and 2.72 nm as shown in Fig. 24(e–h), respectively. Which closely aligns with the values obtained from XRD. Teng et al. [84] reported Pt NPs supported on polyaniline (PANI) and carbon black (CB) with an average particle size of 2.89 nm, demonstrating superior performance compared to Pt supported on carbon black Pt/CB and commercial Pt/C catalysts.

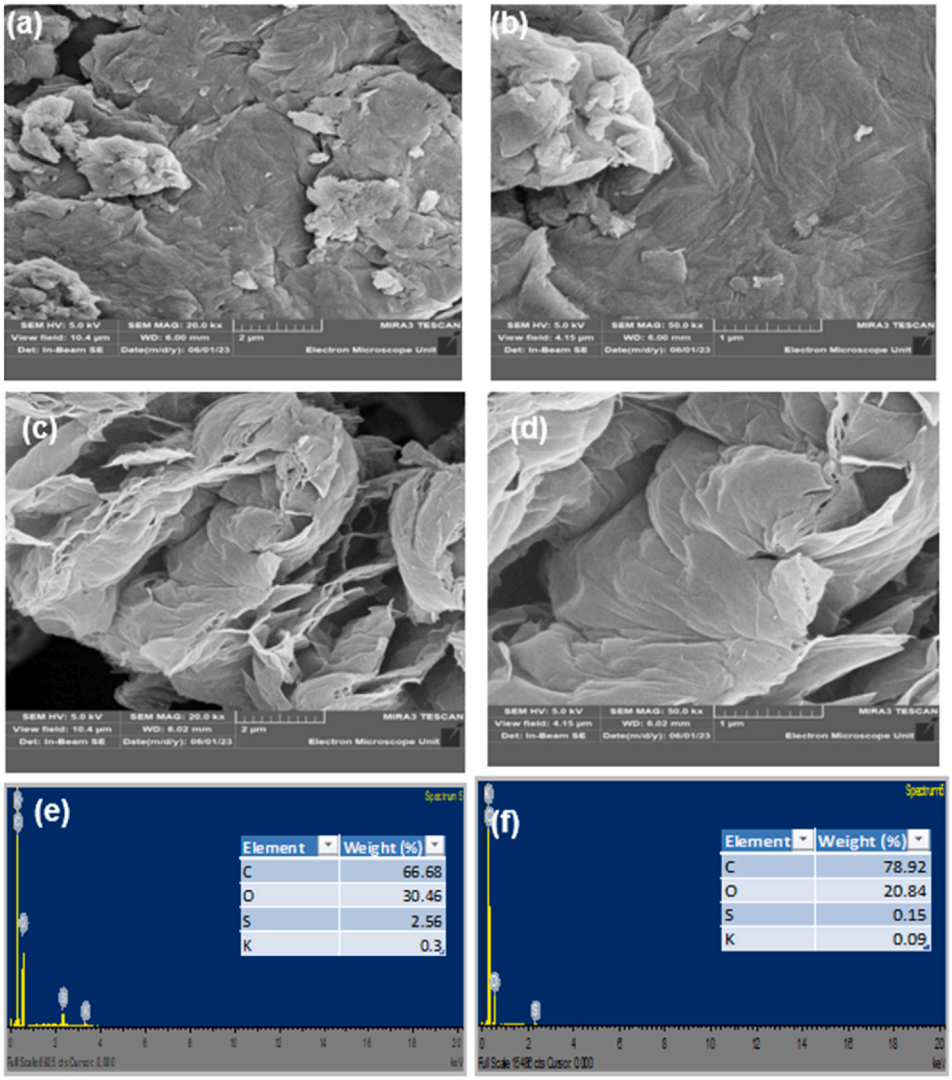

Fig. 21. SEM-EDS micrographs at different magnifications for (a & b) GAC, (c & d) rGO/GAC-1:1, and (e & f) rGO/GAC-1:2.

3.7. Electrochemical analysis

Electrochemical analyses were performed at ambient temperatures using a three-electrode system, which consists of a glassy carbon working electrode, a Pt wire counter electrode, and Ag/AgCl as the reference electrode. The investigated electrochemical techniques were cyclic voltammetry (CV), chronoamperometry (CA), and electrochemical impedance spectroscopy (EIS). The potential window for the CV measurements ranged from −0.300 V to 1.00 V against Ag/AgCl and was covered at 0.03 V/s. The electrolyte utilized was 1 M perchloric acid and 1 M methanol as an alcohol. The solutions were deaerated for 1 h using inert nitrogen gas. The synthesized electrocatalysts that were investigated were Pt-rGO/PAC-1:1, Pt-rGO/PAC-1:2, Pt-rGO/GAC-1:1, and Pt-rGO/GAC-1:2.

3.7.1. Cyclic voltammetry (CV) and electrochemical surface area (ECSA)

Pt-based catalysts are presently the most reliable catalysts for direct methanol fuel cell (DMFCs), and the shape or structure of the catalyst plays a crucial role in influencing its catalytic performance [85]. The CV analysis of the as-prepared Pt-rGO/PAC-1:1, Pt-rGO/PAC-1:2, Pt-rGO/GAC-1:1, and Pt-rGO/GAC-1:2 catalysts was performed in a saturated N_2 atmosphere at 1 M $HClO_4$ solutions at a sweep rate of 0.03 V/s, and the results are shown in Fig. 25.

Two prominent peaks are observed for all catalysts in Fig. 25 in the potential range of −0.28 to −0.13 V. These peaks represent the hydrogen adsorption and desorption processes occurring on the surface of a Pt crystal. The broad feature observed within the anodic region range of 0.04–0.55 V is due to the Faradaic pseudocapacitances linked to the presence of oxygen-containing surface functionalities on the carbon support material, specifically reduced graphene oxide (rGO) [86]. When the potential reached 0.55 V, the Pt metal underwent oxidation, leading to the formation of Pt oxide. Consequently, there is a reduction peak observed at 0.58 V, indicating

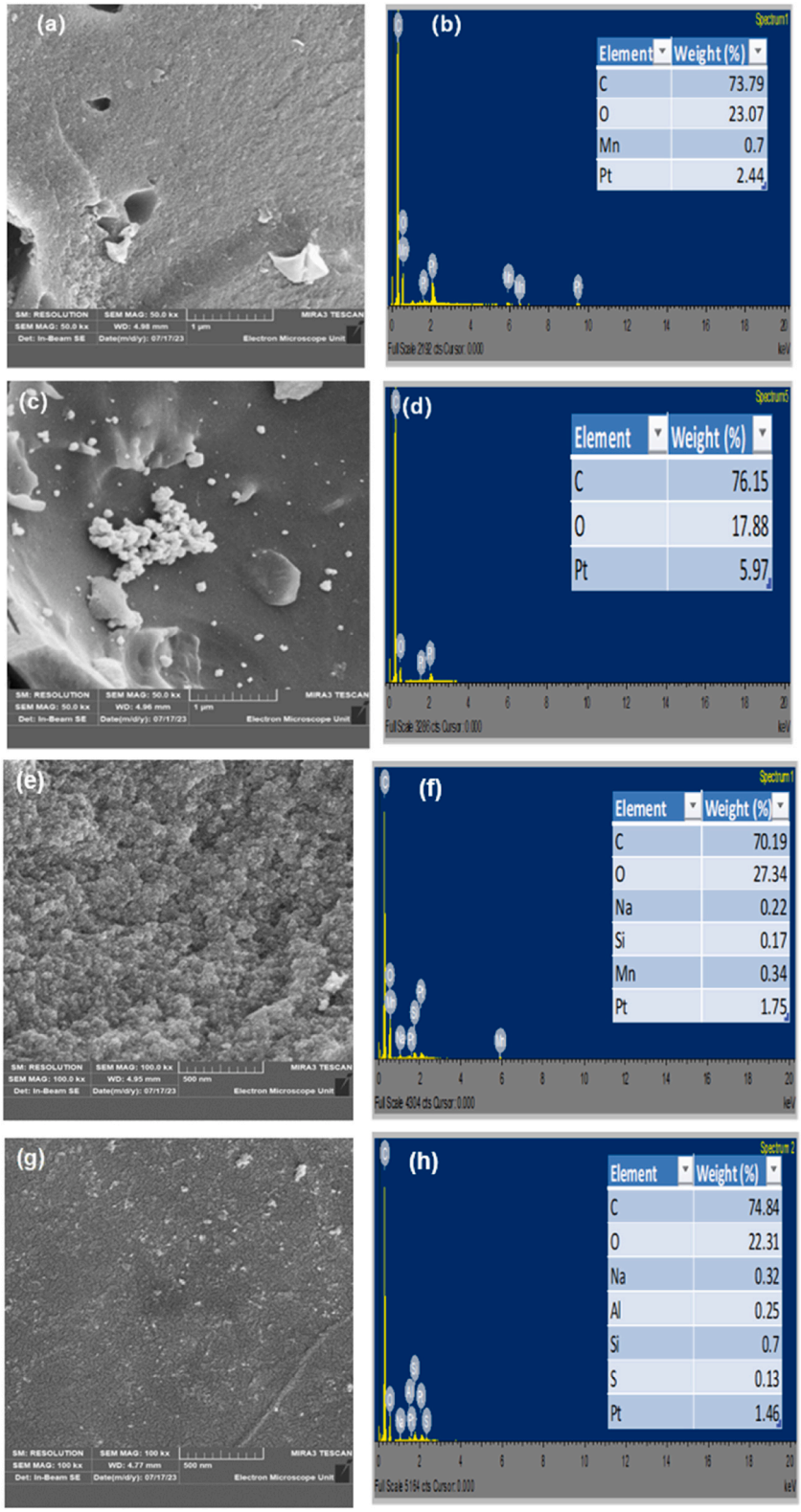

Fig. 22. SEM-EDS micrographs of electrocatalysts at various magnifications for (a & b) Pt-rGO/PAC-1:1, (c & d) Pt-rGO/PAC-1:2, (e & f) Pt-rGO/GAC-1:1, and, (g & h) Pt-rGO/GAC-1:2.

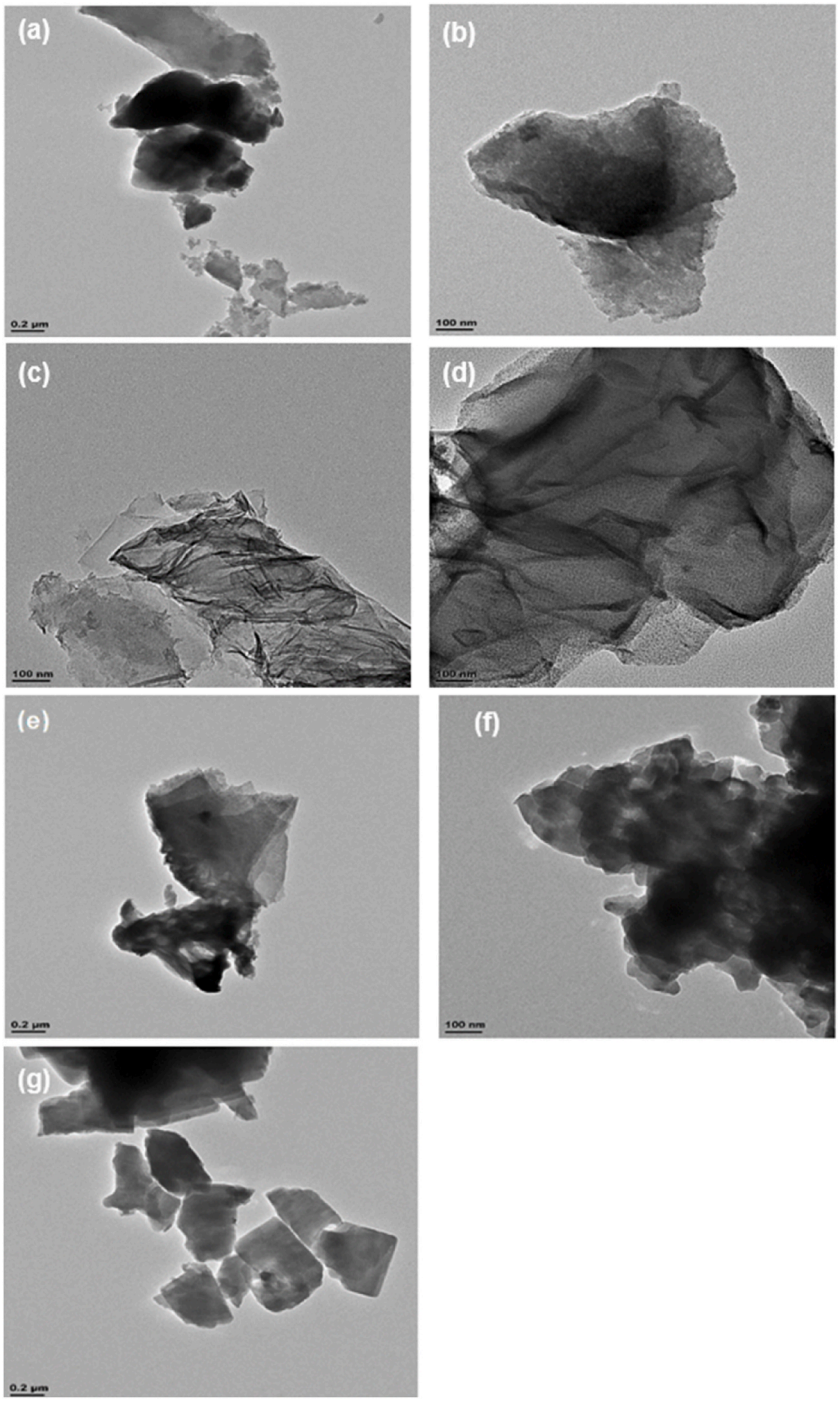

Fig. 23. HRTEM images of (a) GAC, (b) PAC, (c) rGO, (d) rGO/PAC-1:1, (e) rGO/PAC-1:2, (f) rGO/GAC-1:1, and (g) rGO/GAC-1:2 at different magnifications.

the reduction of Pt–O species during the reverse scan.

One of the key parameters used to assess the catalytic activity of these catalysts is the electrochemical active surface area (ECSA), which can be determined through cyclic voltammetry (CV). The ECSA (m^2. g^{-1}) of the catalyst can be calculated (see Equation (5)) as follows [85]:

$$\mathrm{ECSA} = \frac{Q}{\Gamma \times \mathrm{A} \times \mathrm{L}} \tag{5}$$

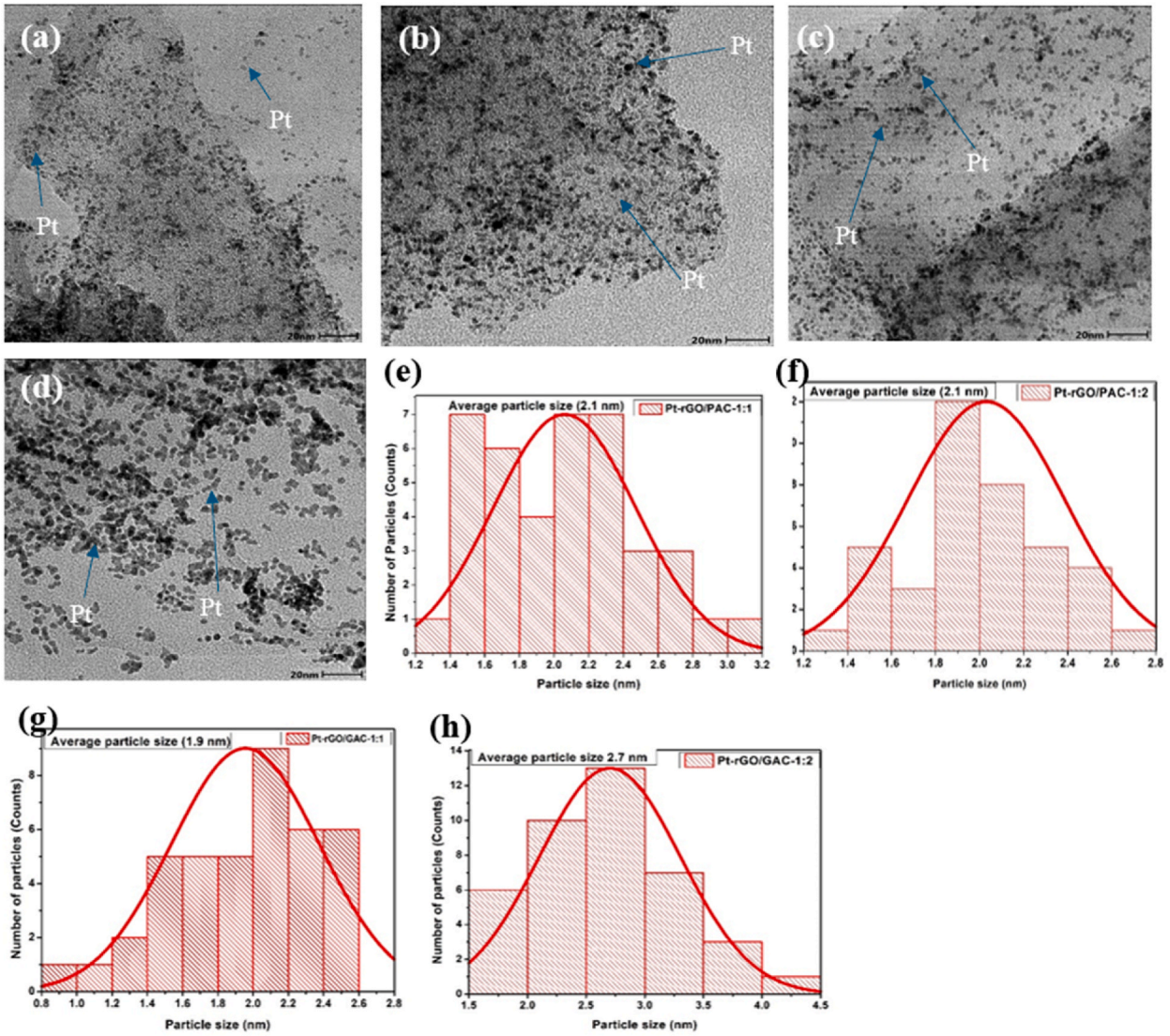

Fig. 24. HRTEM images of (a) Pt-rGO/PAC-1:1, (b) Pt-rGO/PAC-1:2, (c) Pt-rGO/GAC-1:1, and (d) Pt-rGO/GAC-1:2 at 20 nm magnification, and corresponding size histograms of (e) Pt-rGO/PAC-1:1, (f) Pt-rGO/PAC-1:2, (g) Pt-rGO/GAC-1:1, and (h) Pt-rGO/GAC-1:2.

where Q represents the charge from the adsorption peak ($C.m^{-2}$), Γ is the charge to reduce a monolayer of protons on platinum (Γ = 210 μC cm^{-2}), A is the geometric surface area of the glassy carbon electrode (0.196 cm^{-2}) and L is the electrode platinum load ($g_{pt}.m^{-2}$). Table 1 shows the calculated ECSA values for the catalyst.

According to Table 1 above, the ECSA of the as-prepared Pt-rGO/PAC-1:1, Pt-rGO/PAC-1:2, Pt-rGO/GAC-1:1, and Pt-rGO/GAC-1:2 catalysts were calculated to be 30.26 $m^2\ g^{-1}$, 34.37 $m^2\ g^{-1}$, 73.53 $m^2\ g^{-1}$ and 32.49 $m^2\ g^{-1}$. Pt-rGO/GAC-1:1 produced a much larger ECSA than all the as-prepared catalysts suggesting that rGO/GAC-1:1 could expose more catalytically active Pt sites [88]. The low ECSA (30.26 $m^2\ g^{-1}$) value of Pt-rGO/PAC-1:1 is probably due to the intense stacking of the rGO layers during catalyst deposition, and particle agglomeration, or limited accessible active sites [89]. Also, the catalysts produced in this work have higher ECSA values than those reported in the literature [90,91]. The ECSA of the synthesized electrocatalysts outperformed those of the commercial one, as shown in Table 1. The Pt loadings for Pt-rGO/PAC-1:1, Pt-rGO/PAC-1:2, Pt-rGO/GAC-1:1 and Pt-rGO/GAC-1:2 were determined to be 2.62 wt%, 3.71 wt%, 2.23 wt% and 1.96 wt%, respectively. The low Pt content in all the electrocatalysts is due to insufficient anchoring sites on the carbonaceous support to immobilize Pt nanoparticles. Thus, reducing the number of available catalytic sites for MOR [92].

3.7.2. Methanol oxidation reaction

The electroactivity of Pt-rGO/PAC-1:1, Pt-rGO/PAC-1:2, Pt-rGO/GAC-1:1, and Pt-rGO/GAC-1:2 catalysts towards MOR was investigated by CV. Fig. 26 represents the CV curves of Pt-rGO/PAC-1:1, Pt-rGO/PAC-1:2, Pt-rGO/GAC-1:1, and Pt-rGO/GAC-1:2

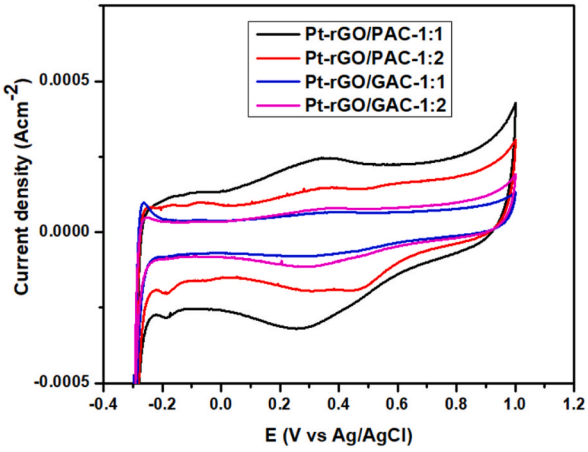

Fig. 25. Cyclic voltammograms (CVs) of Pt-rGO/PAC-1:1, Pt-rGO/PAC-1:2, Pt-rGO/GAC-1:1 and Pt-rGO/GAC-1:2 electrocatalysts in 1 M $HClO_4$ (scan rate at 0.03 V/s).

Table 1
ECSA values of catalysts calculated from cyclic voltammograms and their ICP values.

Catalyst	ECSA ($m^2.g^{-1}$)	ICP (wt%)	Reference
Pt-rGO/PAC-1:1	30.26	2.62	This work
Pt-rGO/PAC-1:2	34.37	3.71	This work
Pt-rGO/GAC-1:1	73.53	2.23	This work
Pt-rGO/GAC-1:2	32.49	1.96	This work
Pt/rGO	21.00	20	[58]
Pt/CB	19.70	22	[59]
PtRu/C	3.25	20	[87]

catalysts saturated in N_2 atmosphere with 1 M $HClO_4$ + CH_3OH solution at a scan rate of 0.03 V/s.

Fig. 26 displays the CV curves of Pt-rGO/PAC-1:1, Pt-rGO/PAC-1:2, Pt-rGO/GAC-1:1, and Pt-rGO/GAC-1:2 electrocatalysts. All the electrocatalysts display both anodic and cathodic peaks in both the forward and reverse scans because of methanol electro-oxidation. The broad peaks observed above 0.4 V in the forward scan indicate the direct oxidation of methanol on the catalyst surface, while the sharp peaks below 0.4 V in the reverse scan are due to the oxidation of carbonaceous intermediates generated during the forward reaction. The low onset potential is an indication of exceptional electrocatalytic activity for methanol oxidation [90]. Scheme 1 shows the enhanced detailed mechanism for MOR occurring on the catalyst surface.

It can be clearly observed in Fig. 26 above that the Pt supported on rGO/PACs has the largest oxidation peaks compared to the Pt supported on rGO/GACs. The peak current densities of Pt-rGO/PAC-1:1 and Pt-rGO/PAC-1:2 are 0.77 and 0.74 $mA*cm^{-2}$ respectively, which are 3.5 times higher than those of Pt-rGO/GAC-1:1 (0.21 $mA*cm^{-2}$) and Pt-rGO/GAC-1:2 (0.24 $mA*cm^{-2}$), see Table 2. These

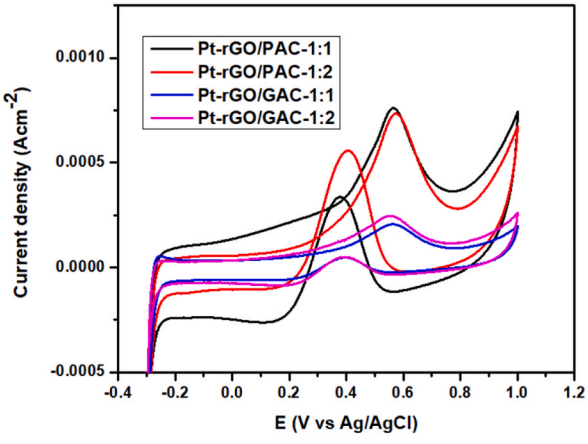

Fig. 26. CV curves of Pt-rGO/PAC-1:1, Pt-rGO/PAC-1:2, Pt-rGO/GAC-1:1, and Pt-rGO/GAC-1:2 electrocatalysts in 1 M $HClO_4$ + CH_3OH solution with a scan rate of 0.03 V/s.

high current densities are due to their high ECSA, Pt-rGO/PAC-1:1 and Pt-rGO/PAC-1:2 exhibit a high number of Pt active sites, coupled with strong electronic interaction between Pt and rGO/PAC supports [93]. The low current densities of Pt-rGO/GAC-1:1 and Pt-rGO/GAC-1:2 might be caused by particle agglomeration on the surface of these catalysts [80], as shown in the HRTEM images in Fig. 24.

The data presented in Table 2 was collected from Fig. 26. The catalytic mass activities of Pt-rGO/PAC-1:1, Pt-rGO/PAC-1:2, Pt-rGO/GAC-1:1, and Pt-rGO/GAC-1:2 were determined using their current densities and the catalyst mass loading. The Pt supported on rGO/PACs showed better electrocatalytic mass activities of 7.55 mA/mg and 7.25 mA/mg, respectively. Which are 3.5 times higher than the mass activities of Pt supported on rGO/GACs, which are 2.06 mA/mg and 2.35 mA/mg, respectively. Additionally, the specific activities of rGO/PAC-1:1, Pt-rGO/PAC-1:2, Pt-rGO/GAC-1:1, and Pt-rGO/GAC-1:2 were calculated to be 0.025 $mA*cm^{-2}$, 0.021 $mA*cm^{-2}$, 0.0028 $mA*cm^{-2}$ and 0.0072 $mA*cm^{-2}$, respectively. Pt supported on rGO/PACs demonstrated to be 2.91 to 8.93 times more electro-catalytic activities compared to Pt supported on rGO/GACs. The ratio I_f/I_r of forward current density to the reverse current density peak can be employed to evaluate the catalyst's ability to tolerate CO, and the ratios are tabulated in Table 2. The Pt-rGO/PAC-1:1, Pt-rGO/PAC-1:2, Pt-rGO/GAC-1:1, and Pt-rGO/GAC-1:2 electrocatalyst have I_f/I_r of about 2.33, 1.38, 5.00 and 5.00, respectively [94].

All electrocatalysts have a high CO tolerance ($I_f/I_r > 1$), showing a lesser number of carbonaceous species formed and better MOR activity. Moreover, based on findings in the literature, it has been documented that in contrast to traditional carbon supports such as carbon black, reduced graphene oxide possesses a greater presence of residual oxygen-containing groups such as epoxide, carboxyl, and hydroxyl groups. These groups have the potential to enhance the conversion of CO-like species into CO_2 [94], and this factor may have played a role in enhancing the methanol oxidation reaction (MOR) activity.

3.7.3. Chronoamperometry

The durability of the prepared catalysts towards MOR was investigated by chronoamperometry for a duration of 3600 s. Fig. 27 shows the chronoamperometry results for Pt-rGO/PAC-1:1, Pt-rGO/PAC-1:2, Pt-rGO/GAC-1:1, and Pt-rGO/GAC-1:2 catalysts in 1 M methanol +1 M $HClO_4$ in a saturated N_2 atmosphere.

Fig. 27 depicts the chronoamperometry results of Pt electrocatalysts supported on rGO/PAC-1:1, rGO/PAC-1:2, rGO/GAC-1:1, and rGO/GAC-1:2, respectively. A rapid decline in the current density of the prepared electrocatalysts is observed as time passes. This rapid decline with time can be attributed to the buildup of CO-like intermediates on the active sites of the electrocatalysts, which in turn inhibits further oxidation of methanol [94]. When comparing the prepared electrocatalyst's stability (see insert), it is evident that the Pt deposited on rGO/PAC-1:2 retained a higher current density with better stability, followed by rGO/PAC-1:1, rGO/GAC-1:2 and lastly rGO/GAC-1:1. This finding implies that PAC is a good support material compared to GAC. The great residual current density of Pt-rGO/PAC-1:2 after 3600 s implies stronger stability and electrochemical activity for methanol oxidation.

3.7.4. Post-chronoamperometry methanol oxidation reaction

Fig. 28 below shows the CV curves of Pt-rGO/PAC-1:1, Pt-rGO/PAC-1:2, Pt-rGO/GAC-1:1 and Pt-rGO/GAC-1:2 catalysts towards MOR after chronoamperometry studies saturated in N_2 atmosphere with 1 M $HClO_4$ + CH_3OH solution at a scan rate of 0.03 V/s.

In Fig. 28, broad apparent current peaks related to methanol oxidation are still detected above 0.4 V, and electro-oxidation removal of carbonaceous intermediate species created in the backward scan is still observed below 0.4 V. After studying the durability of the prepared electrocatalyst (Fig. 27), the peak current densities of Pt-rGO/PAC-1:1, Pt-rGO/PAC-1:2, Pt-rGO/GAC-1:1, and Pt-rGO/GAC-1:2 towards MOR changed to 0.61 $mA*cm^{-2}$, 0.73 $mA*cm^{-2}$, 0.10 $mA*cm^{-2}$ and 0.16 $mA*cm^{-2}$, respectively (see Table 3). These small declines in the current densities suggest that the Pt supported on rGO/PACs can still perform better toward MOR than the Pt supported on rGO/GACs, due to the strong electronic interaction between the Pt and rGO/PACs supports.

The catalytic mass activities of Pt-rGO/PAC-1:1, Pt-rGO/PAC-1:2, Pt-rGO/GAC-1:1, and Pt-rGO/GAC-1:2 also declined to 5.98 mA/mg, 7.15 mA/mg, 0.98 mA/mg and 1.57 mA/mg, respectively, shown in Table 3. Pt-rGO/PAC-1:2 showed better electrocatalytic mass activities, followed by Pt-rGO/GAC-1:1. The ratio of positive-going anodic peak current (I_f) to reverse negative-going anodic peak current (I_r) is a critical index for evaluating CO poisoning catalyst tolerance. In the current study, the I_f/I_r ratios of the Pt-rGO/PAC-1:1, Pt-rGO/PAC-1:2, Pt-rGO/GAC-1:1, and Pt-rGO/GAC-1:2 catalysts were found to be 1.49, 1.52, 3.70, and 6.96, respectively. These ratios (>1) indicate that the as-prepared catalysts are still CO-tolerant even after 1 h of being used.

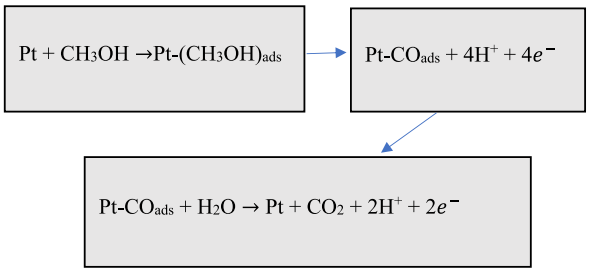

Scheme 1. Detailed mechanism for MOR on the Pt catalyst surface [89].

Table 2
Comparison of the performance of the electrocatalyst towards MOR.

Electrocatalysts	E_{Onset} (V vs Ag/AgCl)	Catalytic Mass activity (mA mg^{-1})	Catalytic Specific activity (mA*cm^{-2})	Peak current density (I_f $_{(oxidation)}$ mA*cm^{-2})	Peak current density (I_r $_{(reduction)}$ mA*cm^{-2})	$\frac{I_f}{I_r}$
Pt-rGO/PAC-1:1	0.40	7.55	0.025	0.77	0.33	2.33
Pt-rGO/PAC-1:2	0.40	7.25	0.021	0.74	0.56	1.38
Pt-rGO/GAC-1:1	0.40	2.06	0.0028	0.21	0.042	5.00
Pt-rGO/GAC-1:2	0.40	2.35	0.0072	0.24	0.048	5.00

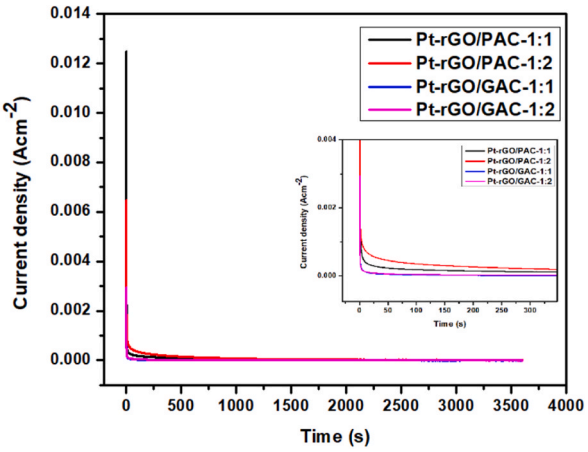

Fig. 27. Chronoamperometry curves of methanol oxidation on Pt-rGO/PAC-1:1, Pt-rGO/PAC-1:2, Pt-rGO/GAC-1:1, and Pt-rGO/GAC-1:2 electrocatalysts in 1 M CH_3OH + 1 M $HClO_4$.

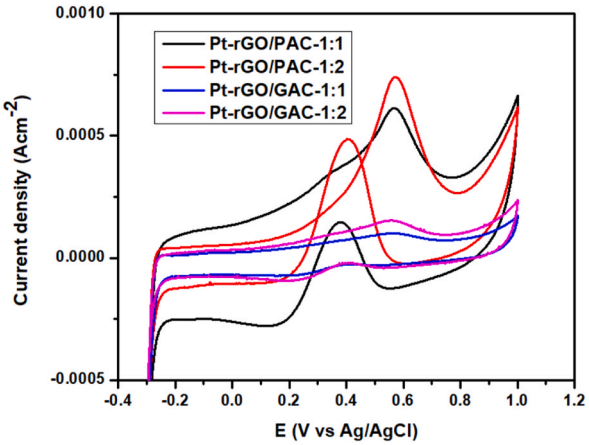

Fig. 28. CV curves of Pt-rGO/PAC-1:1, Pt-rGO/PAC-1:2, Pt-rGO/GAC-1:1, and Pt-rGO/GAC-1:2 electrocatalysts in 1 M $HClO_4$ + CH_3OH solution with a scan rate of 0.03 V/s After chronoamperometry studies.

3.7.5. Electrochemical impedance spectroscopy (EIS)

Electrochemical impedance spectroscopy was used to investigate the kinetics of the catalytic reaction for methanol oxidation on the anodic Pt-rGO/PAC-1:1, Pt-rGO/PAC-1:2, Pt-rGO/GAC-1:1, and Pt-rGO/GAC-1:2 electrocatalyst surfaces. The Nyquist plots of EIS for Pt-rGO/PAC-1:1, Pt-rGO/PAC-1:2, Pt-rGO/GAC-1:1, and Pt-rGO/GAC-1:2 electrocatalysts in 1 M $HClO_4$ + CH_3OH at a saturated N_2 atmosphere are shown in Fig. 29.

As shown in Table 4, the charge transfer resistance (R_{ct}) values for Pt-rGO/PAC-1:1, Pt-rGO/PAC-1:2, Pt-rGO/GAC-1:1, and Pt-rGO/GAC-1:2 electrocatalysts were found to be 14.9 Ω, 14.1 Ω, 15.4 Ω and 17.2 Ω, respectively. Pt-rGO/PAC-1:2 had the lowest

Table 3
Comparison of the performance of the electrocatalyst towards MOR after chronoamperometry.

Electrocatalysts	$E_{Onset(Oxidation)}$ (V vs Ag/AgCl)	Catalytic Mass activity (mA mg^{-1})	Peak current density ($I_{f(oxidation)}$ mA cm^{-2})	Peak current density ($I_{r(reduction)}$ mA cm^{-2})	$\frac{I_f}{I_r}$
Pt-rGO/PAC-1:1	0.4	5.98	0.61	0.41	1.49
Pt-rGO/PAC-1:2	0.4	7.15	0.73	0.48	1.52
Pt-rGO/GAC-1:1	0.4	0.98	0.10	−0.027	3.70
Pt-rGO/GAC-1:2	0.4	1.57	0.16	−0.023	6.96

Rct value (14.1 Ω), indicating superior kinetics for methanol electrooxidation and excellent electrical conductivity. Followed by a Pt-rGO/PAC-1:1 catalyst with an Rct value of 14.9 Ω, showing good electrochemical performance. Thus, Pt-rGO/PAC-1:1 and Pt-rGO/PAC-1:2 electrocatalysts have less difficulty transferring electrons during MOR than Pt-rGO/GAC-1:1 and Pt-rGO/GAC-1:2 electrocatalysts. A high charge-transfer resistance with a low methanol oxidation rate was observed from the Pt-rGo/GAC-1:2 catalyst, as shown in Fig. 29 (insert). The equivalent circuits for EIS of methanol oxidation on Pt-rGO/PAC-1:1, Pt-rGO/PAC-1:2, Pt-rGO/GAC-1:1, and Pt-rGO/GAC-1:2 electrocatalysts are shown in Fig. 30.

4. Conclusions

In summary, four electrocatalysts supported on bio-carbonaceous hybrids were successfully prepared using the microwave-assisted modified polyol method. Initially, GO was synthesized using a modified Hummer's method and thermally converted to rGO at 250 °C for 3 h. The bio-carbonaceous supports, specifically PAC and GAC obtained from Macadamia nuts, were integrated with rGO at varying ratios via the hydrothermal process. Pt NPs were then deposited onto these hybrid supports (rGO/PAC-1:1, rGO/PAC-1:2, rGO/GAC-1:1, and rGO/GAC-1:2) using the microwave-assisted modified polyol method, resulting in Pt-rGO/PAC-1:1, Pt-rGO/PAC-1:2, Pt-rGO/GAC-1:1, and Pt-rGO/GAC-1:2 electrocatalysts. Comprehensive characterization was performed using FTIR, XRD, Raman spectroscopy, TGA, SEM-EDS, HRTEM, CV, chronoamperometry, and EIS techniques.

The calculated crystallite size (D) of Pt-rGO/PAC-1:1, Pt-rGO/PAC-1:2, Pt-rGO/GAC-1:1 & Pt-rGO/GAC-1:2 was found to be 1.36, 1.68, 1.40 and 1.18 nm, respectively. These small sizes significantly contributed to the enhanced electrochemical performance of the catalysts towards MOR. CV results revealed that Pt-rGO/GAC-1:1 possessed the highest electrochemical surface area (ECSA) of 73.53 $m^2\ g^{-1}$, followed by Pt-rGO/PAC-1:2 (34.37 $m^2\ g^{-1}$), Pt-rGO/GAC-1:2 (32.49 $m^2\ g^{-1}$), and Pt-rGO/PAC-1:1 (30.26 $m^2\ g^{-1}$). Despite having the largest electrochemical surface area, Pt-rGO/GAC-1:1 produced the lowest current density of 0.21 mA*cm^{-2} compared to other electrocatalysts, indicating more active sites with less catalytic activity toward MOR. Current densities at an onset potential of 0.4 V were 0.77 mA*cm^{-2}, 0.74 mA*cm^{-2}, and 0.24 mA*cm^{-2} for Pt-rGO/PAC-1:1, Pt-rGO/PAC-1:2 and Pt-rGO/GAC-1:2, respectively. These electrocatalysts demonstrated faster electrochemical reaction kinetics for the electrooxidation of methanol with lower resistance than Pt-rGO/GAC-1:1 and Pt-rGO/GAC-1:2, as evidenced by charge transfer resistance values of 14.9 Ω, 4.1 Ω, 15.4 Ω, and 17.2 Ω, respectively.

Chronoamperometry studies indicated that Pt-rGO/PAC-1:1 and Pt-rGO/PAC-1:2 electrocatalysts exhibited greater stability compared to Pt-rGO/GAC-1:1 and Pt-rGO/GAC-1:2. Following durability tests, Pt-rGO/PAC-1:1 and Pt-rGO/PAC-1:2 catalysts experienced slight drops in current density to 0.61 mA*cm^{-2} and 0.73 mA*cm^{-2} respectively, while Pt-rGO/GAC-1:1 and Pt-rGO/GAC-1:2

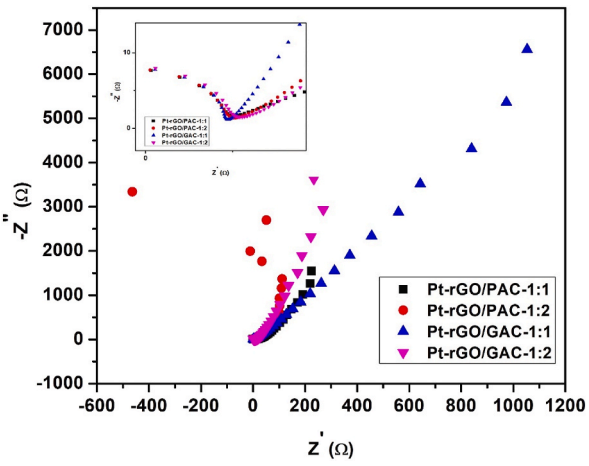

Fig. 29. Nyquist plots for Pt-rGO/PAC-1:1, Pt-rGO/PAC-1:2, Pt-rGO/GAC-1:1, and Pt-rGO/GAC-1:2 electrocatalysts in 1 M $HClO_4$ + CH_3OH at a saturated N_2 atmosphere.

Table 4
Charge transfer resistance (R_{ct}) of the as prepared electrocatalysts.

Catalysts	R_{ct} (charge transfer resistance) in ohms (Ω)
Pt-rGO/PAC-1:1	14.9
Pt-rGO/PAC-1:2	14.1
Pt-rGO/GAC-1:1	15.4
Pt-rGO/GAC-1:2	17.2

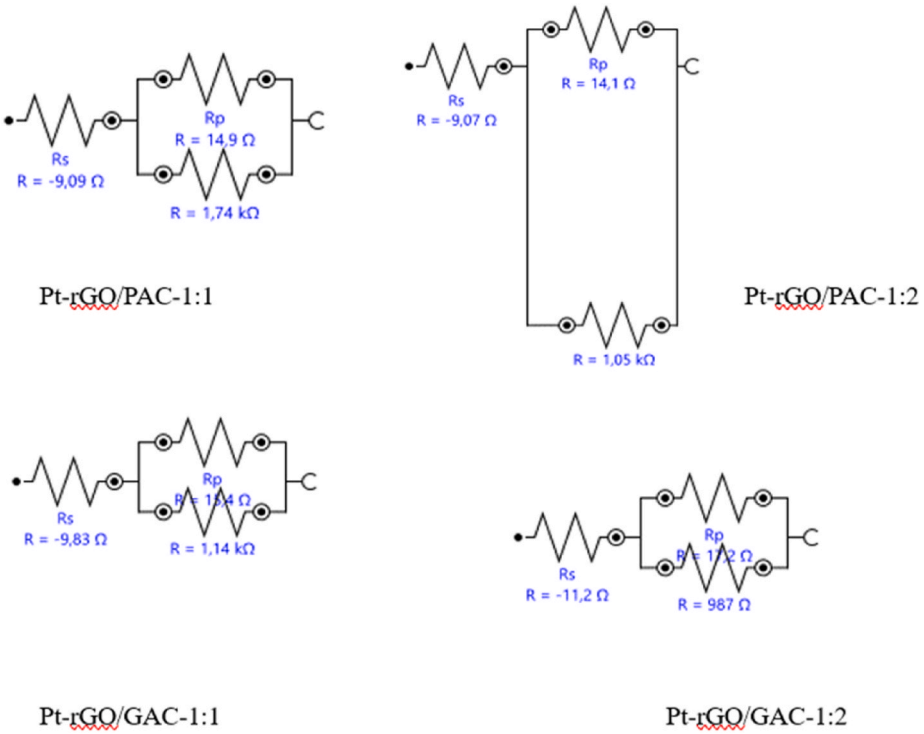

Fig. 30. Equivalent circuits for EIS of methanol oxidation on Pt-rGO/PAC-1:1, Pt-rGO/PAC-1:2, Pt-rGO/GAC-1:1, and Pt-rGO/GAC-1:2 electrocatalysts in 1 M $HClO_4$ + CH_3OH at a saturated N_2 atmosphere. R_p = R_{ct} = Charge transfer resistance estimated from the equivalent circuit.

showed more significant reductions to 0.10 mA*cm^{-2} and 0.16 mA*cm^{-2}, respectively. Based on these findings, Pt-rGO/PACs exhibited superior electrocatalytic activity, kinetics, and stability toward MOR compared to conventional Pt/graphene and Pt/carbon black (Pt/CB) catalysts with equivalent Pt usage, showcasing promising advantages in electrocatalysis.

CRediT authorship contribution statement

N.A. Mojapelo: Writing – original draft, Methodology, Formal analysis, Conceptualization. **N.S. Seroka:** Writing – review & editing, Supervision, Methodology, Formal analysis, Data curation, Conceptualization. **L. Khotseng:** Writing – review & editing, Supervision, Resources, Project administration, Funding acquisition.

Declaration of competing interest

The authors declare that they have no known competing financial interests or personal relationships that could have appeared to influence the work reported in this paper.

Acknowledgement

The financial assistance of the National Research Foundation (NRF) and Eskom, South Africa, towards this research is acknowledged. This research was supported by the Sustainable and Renewable Energy Nanomaterials Research Group, the University of the Western Cape and the Electrochemical Energy Technology Research Group, the Energy Centre at the CSIR, and.

References

[1] T.A. Kurniawan, M.H.D. Othman, X. Liang, H.H. Goh, P. Gikas, T.D. Kusworo, A. Anouzla, K.W. Chew, Decarbonization in waste recycling industry using digitalization to promote net-zero emissions and its implications on sustainability, J. Environ. Manag. 338 (2023) 117765.
[2] T. Yusaf, A.S.F. Mahamude, K. Kadirgama, D. Ramasamy, K. Farhana, H.A. Dhahad, A.R.A. Talib, Sustainable hydrogen energy in aviation–A narrative review, Int. J. Hydrogen Energy 52 (2023) 1026–1045.
[3] S. Aithal, P.S. Aithal, Nanotechnology based mega machine design for large scale air cleaning–prospects and challenges, Int. J. Case Stud. Bus. IT, Educ. (IJCSBE) 4 (2) (2020) 250–269.
[4] Y. Wang, W. Tian, J. Wan, Y. Zheng, H. Zhang, Y. Wang, Tuning coordination microenvironment of V2CTx MXene for anchoring single-atom toward efficient multifunctional electrocatalysis, J. Colloid Interface Sci. 645 (2023) 833–840.
[5] M. Abdullah-Al-Mahbub, A.R.M.T. Islam, H. Almohamad, A.A. Al Dughairi, M. Al-Mutiry, H.G. Abdo, Different forms of solar energy progress: the fast-growing eco-friendly energy source in Bangladesh for a sustainable future, Energies 15 (18) (2022) 6790.
[6] Z.A.C. Ramli, S.K. Kamarudin, Platinum-based catalysts on various carbon supports and conducting polymers for direct methanol fuel cell applications: a review, Nanoscale Res. Lett. 13 (2018) 1–25.
[7] H. Shi, C. Su, R. Ran, J. Cao, Z. Shao, Electrolyte materials for intermediate-temperature solid oxide fuel cells, Prog. Nat. Sci.: Mater. Int. 30 (6) (2020) 764–774.
[8] B. Jaleh, M. Nasrollahzadeh, M. Eslamipanah, A. Nasri, E. Shabanlou, N.R. Manwar, R. Zboril, P. Fornasiero, M.B. Gawande, The role of carbon-based materials for fuel cells performance, Carbon 198 (2022) 301–352.
[9] M.S. Alias, S.K. Kamarudin, A.M. Zainoodin, M.S. Masdar, Active direct methanol fuel cell: an overview, Int. J. Hydrogen Energy 45 (38) (2020) 19620–19641.
[10] L. Wang, Z. Yuan, F. Wen, Y. Cheng, Y. Zhang, G. Wang, A bipolar passive DMFC stack for portable applications, Energy 144 (2018) 587–593.
[11] A.H. Tariq, S.A.A. Kazmi, M. Hassan, S.M. Ali, M. Anwar, Analysis of fuel cell integration with hybrid microgrid systems for clean energy: a comparative review, Int. J. Hydrogen Energy. 52 (2023) 1005–1034.
[12] M. Bayat, S.K. Ergani, Y. Daşdemirli, M. Kayfeci, Fuel cells basics and types, in: Handbook of Thermal Management Systems, Elsevier, 2023, pp. 371–399.
[13] T. Jamal, G.M. Shafiullah, F. Dawood, A. Kaur, M.T. Arif, R. Pugazhendhi, R.M. Elavarasan, S.F. Ahmed, Fuelling the future: an in-depth review of recent trends, challenges and opportunities of hydrogen fuel cell for a sustainable hydrogen economy, Energy Rep. 10 (2023) 2103–2127.
[14] L. Gong, Z. Yang, K. Li, W. Xing, C. Liu, J. Ge, Recent development of methanol electrooxidation catalysts for direct methanol fuel cell, J. Energy Chem. 27 (6) (2018) 1618–1628.
[15] Y. Zuo, W. Sheng, W. Tao, Z. Li, Direct methanol fuel cells system–A review of dual-role electrocatalysts for oxygen reduction and methanol oxidation, J. Mater. Sci. Technol. 114 (2022) 29–41.
[16] C. Yang, Q. Jiang, H. Liu, L. Yang, H. He, H. Huang, W. Li, Pt-on-Pd bimetallic nanodendrites stereoassembled on MXene nanosheets for use as high-efficiency electrocatalysts toward the methanol oxidation reaction, J. Mater. Chem. A 9 (27) (2021) 15432–15440.
[17] L. Mazzapioda, C. Lo Vecchio, A.S. Aricò, M.A. Navarra, V. Baglio, Performance improvement in direct methanol fuel cells by using CaTiO3-δ additive at the cathode, Catalysts 9 (12) (2019) 1017.
[18] M. Borghei, J. Lehtonen, L. Liu, O.J. Rojas, Advanced biomass-derived electrocatalysts for the oxygen reduction reaction, Adv. Mater. 30 (24) (2018) 1703691.
[19] Z.A.C. Ramli, S.K. Kamarudin, Platinum-based catalysts on various carbon supports and conducting polymers for direct methanol fuel cell applications: a review, Nanoscale Res. Lett. 13 (2018) 1–25.
[20] Y. Yu, K. Chen, Q. Wu, Y. Zhang, D. Shi, H. Li, Recent progress on reduced graphene oxide supported Pt-based catalysts and electrocatalytic oxidation performance of methanol, Int. J. Hydrogen Energy 48 (5) (2023) 1785–1812.
[21] D. Liu, L. Li, T. You, Superior catalytic performances of platinum nanoparticles loaded nitrogen-doped graphene toward methanol oxidation and hydrogen evolution reaction, J. Colloid Interface Sci. 487 (2017) 330–335.
[22] J. Thakare, J. Masud, Magnéli TiO2 as a high durability support for the proton exchange membrane (PEM) fuel cell catalysts, Energies 15 (12) (2022) 4437.
[23] F. Chen, Y. Sun, H. Li, C. Li, Review and development of anode electrocatalyst carriers for direct methanol fuel cell, Energy Technol. 10 (6) (2022) 2101086.
[24] W. Meng, H. He, L. Yang, Q. Jiang, B. Yuliarto, Y. Yamauchi, X. Xu, H. Huang, 1D-2D hybridization: nanoarchitectonics for grain boundary-rich platinum nanowires coupled with MXene nanosheets as efficient methanol oxidation electrocatalysts, Chem. Eng. J. 450 (2022) 137932.
[25] L. Wang, M. Gan, L. Ma, X. Hua, X. Li, W. Zhao, Y. Zhang, One-step preparation of polyaniline-modified three-dimensional multilayer graphene supported PtFeOx for methanol oxidation, Synth. Met. 287 (2022) 117068.
[26] W. Wang, X. Zhao, H. Shi, L. Liu, H. Deng, Z. Xu, F. Tian, X. Miao, Shape inducer-free polygonal angle platinum nanoparticles in graphene oxide as oxygen reduction catalyst derived from gamma irradiation, J. Colloid Interface Sci. 575 (2020) 1–15.
[27] Q. Zhang, M.M. Yan, W.F. Du, C.Y. Yin, J. Zhang, L. Yang, Y.Q. Kang, H.Y. He, H.J. Huang, Spatial construction of ultrasmall Pt-decorated 3D spinel oxide-modified N-doped graphene nanoarchitectures as high-efficiency methanol oxidation electrocatalysts, Rare Met. 43 (1) (2024) 186–197.
[28] N.A. Mojapelo, N.S. Seroka, L. Khotseng, Macadamia nut bio-waste: an agricultural waste with potential to Be used as carbon support material in fuel cell applications, Coatings 13 (9) (2023) 1545.
[29] X. Yan, Y. Jia, L. Zhuang, L. Zhang, K. Wang, X. Yao, Defective carbons derived from macadamia nut shell biomass for efficient oxygen reduction and supercapacitors, Chemelectrochem 5 (14) (2018) 1874–1879.
[30] W. Bandason, C. Parwada, A. Mushunje, Macadamia nuts (Macadamia intergrifolia) value chain and technical efficiency among the small-scale farmers in Zimbabwe, Research on World Agricultural Economy 3 (2455–2022-1174) (2022) 25–35.
[31] H. He, R. Zhang, P. Zhang, P. Wang, N. Chen, B. Qian, L. Zhang, J. Yu, B. Dai, Functional carbon from nature: biomass-derived carbon materials and the recent progress of their applications, Adv. Sci. (2023) 2205557.
[32] R. Hidayat, S. Wahyuningsih, A.H. Ramelan, Simple synthesis of rGO (reduced graphene oxide) by thermal reduction of GO (graphene oxide), in: IOP Conference Series: Materials Science and Engineering, vol. 858, IOP Publishing, 2020, June 012009. No. 1.
[33] L.F. Wang, M.M. Geng, X.N. Ding, C. Fang, Y. Zhang, S.S. Shi, Y. Zheng, K. Yang, C. Zhan, X.D. Wang, Research progress of the electrochemical impedance technique applied to the high-capacity lithium-ion battery, Int. J. Miner. Metall. Mater. 28 (2021) 538–552.
[34] V.H. Le, T.H. Nguyen, H.H. Nguyen, L.T.N. Huynh, A.L. Vo, T.K.T. Nguyen, D.T. Nguyen, V.Q. Lam, Fabrication and electrochemical behavior investigation of a Pt-loaded reduced graphene oxide composite (Pt@ rGO) as a high-performance cathode for dye-sensitized solar cells, Int. J. Photoenergy (2020) 1–10, 2020.
[35] T.F. Emiru, D.W. Ayele, Controlled synthesis, characterization and reduction of graphene oxide: a convenient method for large scale production, Egypt. J. Basic Appl. Sci. 4 (1) (2017) 74–79.
[36] S.C. Rodrigues, M.C. Silva, J.A. Torres, M.L. Bianchi, Use of magnetic activated carbon in a solid phase extraction procedure for analysis of 2, 4-dichlorophenol in water samples, Water, Air, Soil Pollut. 231 (2020) 1–13.
[37] R. Hidayat, S. Wahyuningsih, A.H. Ramelan, Simple synthesis of rGO (reduced graphene oxide) by thermal reduction of GO (graphene oxide), in: IOP Conference Series: Materials Science and Engineering, vol. 858, IOP Publishing, 2020, June 012009. No. 1.
[38] X. Lu, K. Xiang, W. Zhou, Y. Zhu, H. Chen, Biomass carbon materials derived from macadamia nut shells for high-performance supercapacitors, Bull. Mater. Sci. 41 (2018) 1–7.
[39] K. Abedi, B. Shahmoradi, E. Mohammadi, K. Wantala, A. Maleki, Y. Zandsalimi, S. Salimi, S. Kohzadi, Photocatalytic degradation of VOCs from air stream using Mo: TiO2/GAC nanocomposites, Mater. Res. Express 9 (2) (2022) 025502.
[40] H.L. Ye, S.X. Liu, C. Zhang, Y.Q. Cai, Y.F. Shi, Dehydrogenation of methylcyclohexane over Pt-based catalysts supported on functional granular activated carbon, RSC Adv. 11 (47) (2021) 29287–29297.
[41] G.S. Avcioglu, B. Ficicilar, A. Bayrakceken, I. Eroglu, High performance PEM fuel cell catalyst layers with hydrophobic channels, Int. J. Hydrogen Energy 40 (24) (2015) 7720–7731.
[42] G. Sreenivasa Kumar, N. Ramamanohar Reddy, B. Sravani, L. Subramanyam Sarma, T. Veera Reddy, V. Madhavi, S. Adinarayana Reddy, Ultra-range bimetallic Pt–Pd nanospheres deposited on reduced graphene sheet as efficient electrocatalyst towards electrooxidation of methanol, J. Cluster Sci. 32 (2021) 27–36.

[43] C.H. Manoratne, S.R.D. Rosa, I.R.M. Kottegoda, XRD-HTA, UV visible, FTIR and SEM interpretation of reduced graphene oxide synthesized from high purity vein graphite, Mater. Sci. Res. Int. 14 (1) (2017) 19–30.

[44] T.F. Emiru, D.W. Ayele, Controlled synthesis, characterization and reduction of graphene oxide: a convenient method for large scale production, Egypt. J. Basic Appl. Sci. 4 (1) (2017) 74–79.

[45] K. Melaphi, O.O. Sadare, G.S. Simate, S. Wagenaar, K. Moothi, Adsorptive removal of BTEX compounds from wastewater using activated carbon derived from macadamia nut shells, WaterSA 49 (1) (2023) 36–45.

[46] N. Mojoudi, N. Mirghaffari, M. Soleimani, H. Shariatmadari, C. Belver, J. Bedia, Phenol adsorption on high microporous activated carbons prepared from oily sludge: equilibrium, kinetic and thermodynamic studies, Sci. Rep. 9 (1) (2019) 19352.

[47] J.N. Edokpayi, S.O. Alayande, A. Adetoro, J.O. Odiyo, The Equilibrium, kinetics, and thermodynamics studies of the sorption of methylene blue from aqueous solution using pulverized raw macadamia nut shells, J. Anal. Methods Chem. 2020 (2020).

[48] S. Wongcharee, V. Aravinthan, L. Erdei, W. Sanongraj, Mesoporous activated carbon prepared from macadamia nut shell waste by carbon dioxide activation: comparative characterisation and study of methylene blue removal from aqueous solution, Asia Pac. J. Chem. Eng. 13 (2) (2018) e2179.

[49] M.J. Phele, I.P. Ejidike, F.M. Mtunzi, Adsorption efficiency of activated macadamia nutshell for the removal Organochlorine pesticides: endrin and 4, 4-DDT from aqueous solution, J. Pharmaceut. Sci. Res. 11 (1) (2019) 258–262.

[50] N. Mojoudi, N. Mirghaffari, M. Soleimani, H. Shariatmadari, C. Belver, J. Bedia, Phenol adsorption on high microporous activated carbons prepared from oily sludge: equilibrium, kinetic and thermodynamic studies, Sci. Rep. 9 (1) (2019) 19352.

[51] H.H. Nekhavhambe, R. Mudzielwana, M.W. Gitari, W.B. Ayinde, O.U. Izevbekhai, Fluoride bio-sorption efficiency and antimicrobial potency of macadamia nut shells, Materials 15 (3) (2022) 1065.

[52] S. Thakur, N. Karak, Green reduction of graphene oxide by aqueous phytoextracts, Carbon 50 (14) (2012) 5331–5339.

[53] V. Loryuenyong, K. Totepvimarn, P. Eimburanapravat, W. Boonchompoo, A. Buasri, Preparation and characterization of reduced graphene oxide sheets via water-based exfoliation and reduction methods, Adv. Mater. Sci. Eng. 2013 (2013).

[54] S. Esabattina, V.R. Posa, H. Zhanglian, S. kumar Godlaveeti, R.R.N. Reddy, A.R. Somala, Fabrication of bimetallic PtPd alloy nanospheres supported on rGO sheets for superior methanol electro-oxidation, Int. J. Hydrogen Energy 43 (8) (2018) 4115–4124.

[55] Y.T. Lai, W.T. Liu, L.C. Chung, P.I. Liu, M.C. Chang, R.Y. Horng, L.J. Chen, C.Y. Lee, N.H. Tai, A facile microwave-assisted method to prepare highly electrosorptive reduced graphene oxide/activated carbon composite electrode for capacitive deionization, Adv. Mater. Technol. 4 (9) (2019) 1900213.

[56] Q.A. Khan, A. Shaur, T.A. Khan, Y.F. Joya, M.S. Awan, Characterization of reduced graphene oxide produced through a modified Hoffman method, Cogent Chem. 3 (1) (2017) 1298980.

[57] N.M.S. Hidayah, W.W. Liu, C.W. Lai, N.Z. Noriman, C.S. Khe, U. Hashim, H.C. Lee, Comparison on graphite, graphene oxide and reduced graphene oxide: synthesis and characterization, in: AIP Conference Proceedings, vol. 1892, AIP Publishing, 2017, October. No. 1.

[58] L. Xu, Y. Li, M. Jia, Q. Zhao, X. Jin, C. Yao, Synthesis and characterization of free-standing activated carbon/reduced graphene oxide film electrodes for flexible supercapacitors, RSC Adv. 7 (71) (2017) 45066–45074.

[59] J. Zhang, T. Tian, Y. Chen, Y. Niu, J. Tang, L.C. Qin, Synthesis of graphene from dry ice in flames and its application in supercapacitors, Chem. Phys. Lett. 591 (2014) 78–81.

[60] M.K. Sahoo, G.R. Rao, Enhanced methanol electro-oxidation activity of Pt/rGO electrocatalyst promoted by NbC/Mo2C phases, ChemistrySelect 5 (13) (2020) 3805–3814.

[61] F.E. Che Othman, N. Yusof, J. González-Benito, X. Fan, A.F. Ismail, Electrospun composites made of reduced graphene oxide and polyacrylonitrile-based activated carbon nanofibers (rGO/ACNF) for enhanced CO2 adsorption, Polymers 12 (9) (2020) 2117.

[62] P. Ndagijimana, X. Liu, Q. Xu, D. Lai, G. Wang, B. Pan, Y. Wang, Cassava flour extracts solution to induce gelatin cross-linked activated carbon-graphene oxide composites: the adsorption performance of dyes from aqueous media, Environ. Adv. 5 (2021) 100079.

[63] M. Muhyuddin, N. Zocche, R. Lorenzi, C. Ferrara, F. Poli, F. Soavi, C. Santoro, Valorization of the inedible pistachio shells into nanoscale transition metal and nitrogen codoped carbon-based electrocatalysts for hydrogen evolution reaction and oxygen reduction reaction, Mater. Renew. Sustain. Energy 11 (2) (2022) 131–141.

[64] N.M.S. Hidayah, W.W. Liu, C.W. Lai, N.Z. Noriman, C.S. Khe, U. Hashim, H.C. Lee, Comparison on graphite, graphene oxide and reduced graphene oxide: synthesis and characterization, in: AIP Conference Proceedings, vol. 1892, AIP Publishing, 2017, October. No. 1.

[65] N. Pongpichayakul, P. Waenkeaw, J. Jakmunee, S. Themsirimongkon, S. Saipanya, Activity and stability improvement of platinum loaded on reduced graphene oxide and carbon nanotube composites for methanol oxidation, J. Appl. Electrochem. 50 (2020) 51–62.

[66] T. Tene, G. Tubon Usca, M. Guevara, R. Molina, F. Veltri, M. Arias, L.S. Caputi, C. Vacacela Gomez, Toward large-scale production of oxidized graphene, Nanomaterials 10 (2) (2020) 279.

[67] G.B. Mahendran, S.J. Ramalingam, J.B.B. Rayappan, S. Kesavan, T. Periathambi, N. Nesakumar, Green preparation of reduced graphene oxide by Bougainvillea glabra flower extract and sensing application, J. Mater. Sci. Mater. Electron. 31 (2020) 14345–14356.

[68] Y.M. Ahmed, A.A. Al-Mamun, S.A. Muyibi, M.F.R. Al-Khatib, A.T. Jameel, M.A. AlSaadi, The formation of carbon nanofibers on powdered activated carbon impregnated with nickel, in: AIP Conference Proceedings, vol. 1136, American Institute of Physics, 2009, June, pp. 519–522. No. 1.

[69] J. Zhao, T. Liu, H. Shi, J. Zhang, H. Li, W. Ge, Y. Chi, Preparation and characterization of MnO2-impregnated granular activated carbon for Reactive Black 5 removal, Desalination Water Treat. 171 (2019) 428–435.

[70] B. Jonas, R. Mwemezi, K. Mtei, Adsorption and Desorption Ability of Divalent Mercury from an Interactive Bicomponent Sorption System Using Hybrid Granular Activated Carbon, 2023.

[71] K. Noel, *Study of Pt-M (M= Au and Co) Nano-Catalysts with Low Pt Loading for PEMFC Applications* (Doctoral Dissertation), 2010.

[72] M. Bera, P. Gupta, P.K. Maji, Facile one-pot synthesis of graphene oxide by sonication assisted mechanochemical approach and its surface chemistry, J. Nanosci. Nanotechnol. 18 (2) (2018) 902–912.

[73] N. Kumar, K. Setshedi, M. Masukume, S.S. Ray, Facile scalable synthesis of graphene oxide and reduced graphene oxide: comparative investigation of different reduction methods, Carbon Lett. 32 (4) (2022) 1031–1046.

[74] N.M.S. Hidayah, W.W. Liu, C.W. Lai, N.Z. Noriman, C.S. Khe, U. Hashim, H.C. Lee, Comparison on graphite, graphene oxide and reduced graphene oxide: synthesis and characterization, in: AIP Conference Proceedings, vol. 1892, AIP Publishing, 2017, October. No. 1.

[75] C.H.V. Brito, D.C.S. Gloria, E.B. Santos, R.A. Domingues, G.T. Valente, N.C.S. Vieira, M. Gonçalves, Porous activated carbon/graphene oxide composite for efficient adsorption of pharmaceutical contaminants, Chem. Eng. Res. Des. 191 (2023) 387–400.

[76] J. Wang, Q. Li, C. Peng, N. Shu, L. Niu, Y. Zhu, To increase electrochemical performance of electrode material by attaching activated carbon particles on reduced graphene oxide sheets for supercapacitor, J. Power Sources 450 (2020) 227611.

[77] H.Y. Jung, Y.R. Kim, H.T. Jeong, All-solid-state supercapacitor composed of reduced graphene oxide (rGO)/activated carbon (AC) composite and polymer electrolyte, Carbon Lett. 30 (2020) 107–113.

[78] R. Joshi, A. De Adhikari, A. Dey, I. Lahiri, Green reduction of graphene oxide as a substitute of acidic reducing agents for supercapacitor applications, Mater. Sci. Eng., B 287 (2023) 116128.

[79] D. Mohan, A. Sarswat, V.K. Singh, M. Alexandre-Franco, C.U. Pittman Jr, Development of magnetic activated carbon from almond shells for trinitrophenol removal from water, Chem. Eng. J. 172 (2–3) (2011) 1111–1125.

[80] O. Folorunso, R. Sadiku, Y. Hamam, S.S. Ray, An investigation of copper oxide-loaded reduced graphene oxide nanocomposite for energy storage applications, Appl. Phys. A 128 (1) (2022) 54.

[81] Z. Yang, X. Ju, H. Liao, Z. Meng, H. Ning, Y. Li, Z. Chen, J. Long, Preparation of activated carbon doped with graphene oxide porous materials and their high gas adsorption performance, ACS Omega 6 (30) (2021) 19799–19810.

[82] X. Wang, C. Jiang, J. Wang, K. Gui, H.R. Thomas, Promoted dispersion and uniformity of active species on Fe–Ce–Al catalysts for efficient NO abatement, RSC Adv. 9 (61) (2019) 35751–35759.

[83] J. Cai, Z. Yu, J. Li, Effect of preparation methods on the performance of Pt/TiO2 catalysts for the catalytic oxidation of carbon monoxide in simulated sintering flue gas, Catalysts 11 (7) (2021) 804.
[84] Z. Teng, Z. Zhang, X. Li, Preparation of Pt catalysts supported on polyaniline modified carbon black and electrocatalytic methanol oxidation, Synth. Met. 293 (2023) 117256.
[85] W. Duan, A. Li, Y. Chen, J. Zhang, K. Zhuo, Amino acid-assisted preparation of reduced graphene oxide-supported PtCo bimetallic nanospheres for electrocatalytic oxidation of methanol, J. Appl. Electrochem. 49 (2019) 413–421.
[86] D. He, K. Cheng, T. Peng, X. Sun, M. Pan, S. Mu, Bifunctional effect of reduced graphene oxides to support active metal nanoparticles for oxygen reduction reaction and stability, J. Mater. Chem. 22 (39) (2012) 21298–21304.
[87] S.H. Osman, S.K. Kamarudin, S. Basri, N.A. Karim, Anodic catalyst support via titanium dioxide-graphene aerogel (TiO2-GA) for A direct methanol fuel cell: response surface approach, Catalysts 13 (6) (2023) 1001.
[88] H. Huang, Y. Wei, Y. Yang, M. Yan, H. He, Q. Jiang, X. Yang, J. Zhu, Controllable synthesis of grain boundary-enriched Pt nanoworms decorated on graphitic carbon nanosheets for ultrahigh methanol oxidation catalytic activity, J. Energy Chem. 57 (2021) 601–609.
[89] M.K. Sahoo, G.R. Rao, Enhanced methanol electro-oxidation activity of Pt/rGO electrocatalyst promoted by NbC/Mo2C phases, ChemistrySelect 5 (13) (2020) 3805–3814.
[90] J. Zhao, L. Zhang, T. Chen, H. Yu, L. Zhang, H. Xue, H. Hu, Supercritical carbon-dioxide-assisted deposition of Pt nanoparticles on graphene sheets and their application as an electrocatalyst for direct methanol fuel cells, J. Phys. Chem. C 116 (40) (2012) 21374–21381.
[91] L.P. Hoe, M. Boaventura, T. Lagarteira, L.K. Shyuan, A. Mendes, Polyol synthesis of reduced graphene oxide supported platinum electrocatalysts for fuel cells: effect of Pt precursor, support oxidation level and pH, Int. J. Hydrogen Energy 43 (35) (2018) 16998–17011.
[92] M. Fan, L. Cui, X. He, X. Zou, Emerging heterogeneous supports for efficient electrocatalysis, Small Methods 6 (10) (2022) 2200855.
[93] K. Huang, J. Zhong, J. Huang, H. Tang, Y. Fan, M. Waqas, B. Yang, W. Chen, J. Yang, Fine platinum nanoparticles supported on polyindole-derived nitrogen-doped carbon nanotubes for efficiently catalyzing methanol electrooxidation, Appl. Surf. Sci. 501 (2020) 144260.
[94] G. Sreenivasa Kumar, N. Ramamanohar Reddy, B. Sravani, L. Subramanyam Sarma, T. Veera Reddy, V. Madhavi, S. Adinarayana Reddy, Ultra-range bimetallic Pt–Pd nanospheres deposited on reduced graphene sheet as efficient electrocatalyst towards electrooxidation of methanol, J. Cluster Sci. 32 (2021) 27–36.